

# **Picosecond transfer from short-term to long-term memory in analog antiferromagnetic memory device**

M. Surýnek<sup>1,\*</sup>, J. Zubáč<sup>2,1,\*</sup>, K. Olejník<sup>2</sup>, A. Farkaš<sup>2,1</sup>, F. Křížek<sup>2</sup>, L. Nádvorník<sup>1</sup>, P. Kubaščík<sup>1</sup>, F. Trojánek<sup>1</sup>, R.P. Champion<sup>3</sup>, V. Novák<sup>2</sup>, T. Jungwirth<sup>2,3</sup>, and P. Němec<sup>1,†</sup>

<sup>1</sup>Faculty of Mathematics and Physics, Charles University, Ke Karlovu 3, 121 16 Prague 2, Czech Republic

<sup>2</sup>Institute of Physics ASCR, v.v.i., Cukrovarnická 10, 162 53 Prague 6, Czech Republic

<sup>3</sup>School of Physics and Astronomy, University of Nottingham, Nottingham NG7 2RD, United Kingdom

**Experiments in materials with a compensated ordering of magnetic moments have demonstrated a potential for approaching the thermodynamic limit of the fastest and least-dissipative operation of a digital memory bit. In addition, these materials are very promising for a construction of energy-efficient analog devices with neuromorphic functionalities, which are inspired by computing-in-memory capabilities of the human brain. In this paper, we report on experimental separation of switching-related and heat-related resistance signal dynamics in memory devices microfabricated from CuMnAs antiferromagnetic metal. We show that the memory's variable multilevel resistance can be used as a long-term memory (LTM), lasting up to minutes at room temperature. In addition, ultrafast reflectivity change and heat dissipation from nanoscale-thickness CuMnAs films, taking place on picosecond to hundreds of nanoseconds time scales, can be used as a short-term memory (STM). Information about input stimuli, represented by femtosecond laser pulses, can be transferred from STM to LTM after rehearsals at picosecond to nanosecond times in these memory devices, where information can be retrieved at times up to  $10^{15}$  longer than the input pulse duration. Our results open a route towards ultra-fast low-power implementations of spiking neuron and synapse functionalities using a resistive analog antiferromagnetic memory.**

---

\* These authors contributed equally.

† Electronic mail: petr.nemec@matfyz.cuni.cz

The internal spin-dynamics in crystals with a compensated antiparallel ordering of magnetic moments is commonly in the ps (THz) range [1]. It makes these systems favorable for a demonstration of a memory technology approaching at room temperature the Landauer  $\sim$  meV limit, combined with the corresponding  $\sim$  ps temporal limit, of the least-dissipative and fastest operation of a digital bit [2,3]. A ps-scale Néel vector reorientation from a stable easy axis to a transiently excited distinct easy axis at energy of  $\sim$  meV per atom was demonstrated using a THz-field pulse in an insulating magnetically-compensated orthoferrite [4]. By employing a Néel spin-orbit torque excitation in metallic antiferromagnets, a method originally introduced in studies of electrical switching [5-7], it has been recently shown that a ps-scale switching between two stable Néel-vector orientations can be achieved by a THz field pulse at an energy of  $\sim$  10 meV per atom [8]. Without a significant increase of the threshold excitation energy for switching, compared to the bi-stable spin-orbit torque switching, the metallic antiferromagnetic devices can be also operated as an analog memory featuring a continuous range of metastable variable resistance states [9-12].

Apart from applications in spintronics [1,13,14], antiferromagnets hold many promises also for bio-inspired neuromorphic computing [15-19]. In conventional von Neumann computing architecture, digital data processing and storage are performed in mutually-independent functional parts. In contrast, in human brain, where  $\sim 10^{11}$  neurons are interconnected by  $\sim 10^{15}$  synapses [20,21], data processing is performed by the computing-in-memory architecture in a highly parallel and energy-efficient manner. On a cellular level, memories are stored by modifying the synaptic strengths, which can be increased or decreased, depending on the previous activity patterns – the very active synapses are likely to become stronger, and those that are less active tend to become weaker [22,23]. According to timescales, the synaptic activity can be divided into short-term plasticity [23-26] and long-term plasticity [27-29]. In fact, this division is not only about time, it is also connected with different roles that synaptic activity plays in neural circuits. The long-term potentiation (i.e., a synaptic strength increase) and long-term depression (a synaptic strength decrease), happening on the time scale of seconds and longer, are believed to constitute the basics of learning and memory. In contrast, the short-term plasticity, which takes place from milliseconds to seconds, form the basis for advanced neuromorphic functions, including sound localization, associative learning and working memory [30,31]. On a system level, the most accepted model of human memory and forgetting is the multistore model [32]. In this model, new information is stored in short-term memory (STM) first and it is transferred to long-term memory

(LTM) through a process of rehearsal, where the transfer probability increases with rehearsal repetitions [33-35]. Overall, the existence of synaptic activities at two markedly different timescales seems to be essential for achieving the cognitive tasks and low-power computing capabilities of the human brain.

In this paper, we demonstrate that resistive memory devices based on antiferromagnetic metal CuMnAs possess both STM and LTM-functionalities and information can be transferred from STM to LTM upon rehearsals at ultrashort time scales. As the input stimuli, we use bursts consisting of 1 to 16 femtosecond laser pulses. In the devices, STM is based on ultrafast heat and transient reflectivity dynamics in nanometer-thin CuMnAs films, which is generic to many materials. However, the favorable feature of CuMnAs is that it can be switched by the accumulated heat to a continuous range of metastable variable resistance states, with a relative resistance-change reaching  $\sim 10\%$  at room temperature and  $\sim 100\%$  at low temperatures [10-12]. High-resolution microscopy studies ascribed these metastable variable resistance states, which can be detected at times up to  $10^{15}$  longer than the input laser pulse duration, to a formation of unconventional nano-scale magnetic textures in the compensated antiferromagnet [12,36].

## RESULTS

### Samples and experimental setup

Epilayers of tetragonal CuMnAs with a thickness from 8 to 60 nm were grown by molecular beam epitaxy on a lattice matched GaP substrate [37]. Electron-beam lithography and wet chemical etching were predominantly used to pattern the devices [12]. (For more details on the sample preparation see Methods.) In the measurements, we employ a broad range of experimental techniques of ultrafast laser spectroscopy. In particular, we use a "multiplier" of laser pulses to produce bursts of equiamplitude laser pulses, with each burst containing 1, 2, 4, 8, or 16 pulses, from a single 150 fs long laser pulse with a user-selectable equidistant time delay between pulses. These bursts serve as input stimuli to excite studied devices, whose electrical resistance is measured in a real-time domain. To experimentally separate device resistance changes due to the temperature increase and switching in CuMnAs, we use a stroboscopic optical-pump/electrical-probe method using a high-performance oscilloscope with a 6 GHz bandwidth and 150 fs laser pulses, or pairs of laser pulses of equal fluence and precisely controlled mutual time delay in a range from (sub)picoseconds to nanoseconds. Finally, we used all-optical pump-probe experiments to measure independently the electron-phonon relaxation time in CuMnAs and the

heat dissipation from CuMnAs film to substrate, which strongly depends on the CuMnAs film thickness. (For more details on the experimental techniques see Methods and Supplementary information, Part A.)

### STM to LTM information transfer

In Figs. 1a to 1d we schematically depict the similarities between a biological synapse and CuMnAs-based memory device. In the device, STM is accomplished by heat dissipation from nanometer-thin CuMnAs film (see Fig. 1c), which is happening on a time scale from picoseconds to hundreds of nanoseconds after absorption of a femtosecond laser pulse. On longer time scales, from tens of nanoseconds to minutes at room temperature, the laser-induced device resistance changes due to the multi-level switching (see Fig. 1d), playing the role of LTM, can be separated from the heating-induced resistance changes. In Fig. 1e we show the multistore model of human memory depicting that information about input stimulus, provided by a "sensor", is transferred from STM to LTM only after a frequent rehearsal [32]. As we demonstrate in Figs. 1f to 1h, an analogous functionality can be realized in our CuMnAs-based memory device. We use femtosecond laser pulses with a selectable number of pulses in each burst as input stimuli (see Methods and Figs. S1c to S1f in Supplementary information, part A) and absorption in CuMnAs as a "sensor". If the number of laser pulses (i.e., the rehearsal number) is increasing, the transiently accumulated temperature in the CuMnAs film is increasing, as depicted in Fig. 1g. Eventually, when the switching threshold is reached, nano-scale magnetic textures in CuMnAs are formed which, in turn, leads to a device resistance increase [12,36], electrically detectable on extended times (Fig. 1h). A further increase of laser pulses number increases the volume of the material where the switching threshold is overpassed (see Supplementary Fig. S2 and the corresponding text in Supplementary information, part B) and, therefore, the measured device resistance increases.

As we show later in this paper, the heat dissipation dynamics in CuMnAs films after absorption of a femtosecond laser pulse take place on several distinct time scales. The dominant processes, which are exploited in Figs. 1 a 2, can be approximated by a sum of three exponential decay functions with characteristic time constants  $\tau_i$  (and amplitudes  $A_i$ ). Time constant  $\tau_1$  (with amplitude  $A_1 \sim 0.67$ ), which describes a heat transfer from the CuMnAs film to the GaP substrate, depends strongly on the film thickness and it reaches  $\sim 400$  and  $1\ 300$  ps in the 20 and 50 nm films, respectively. (The whole measured thickness dependence of  $\tau_1$  is shown in the inset of Fig. 4f). On the other hand, time constants  $\tau_2 \sim 10$  ns ( $A_2 \sim 0.25$ ) and  $\tau_3 \sim 100$  ns ( $A_3 \sim 0.08$ ), which we attributed

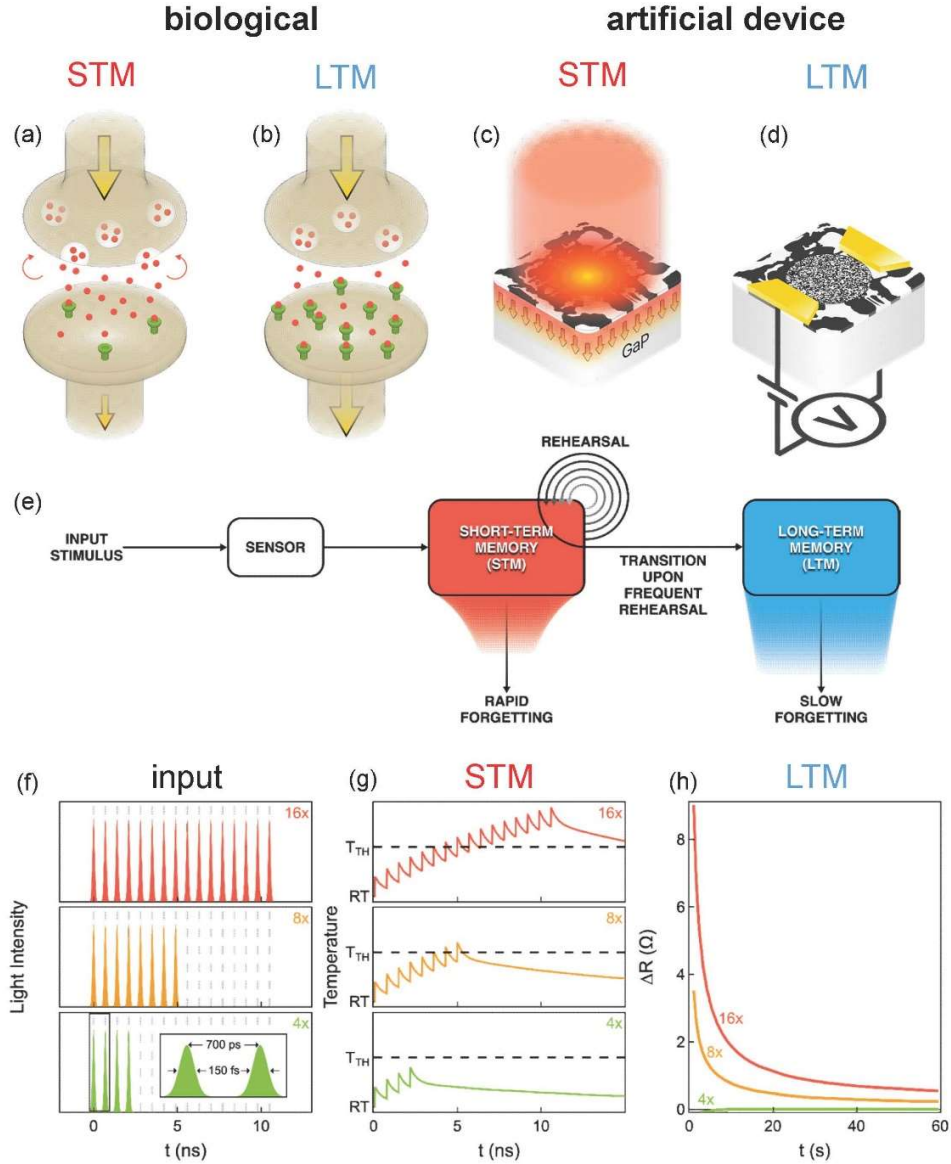


**Figure 1: Demonstration of information transfer from ultrafast short-term memory (STM) to long-term memory (LTM) in analog antiferromagnetic CuMnAs memory device.**

**a**, In a biological synapse, the presynaptic and postsynaptic neurons are separated by a 20–40 nm thick gap, known as a synaptic cleft. The transient change of a synaptic weight, responsible for a short-term memory (STM) on a time scale from milliseconds to seconds, is mediated by neurotransmitters released by the presynaptic neuron. **b**, The increase of a number of postsynaptic receptors (depicted in green) on longer time scales, from tens of seconds onwards, leads to a long-term memory (LTM). **c** and **d**, Schematic of CuMnAs-based memory device where the ultrafast reflectivity change and heat dissipation from CuMnAs layer (red arrows) after excitation by a single femtosecond laser pulse (red column) play the role of STM and the device resistance increase plays the role of LTM. **e**, Multistore model of human memory [32] illustrating that information from a "sensor" is transferred from STM to LTM only after a frequent rehearsal. **f**, In the device, laser pulse bursts are used as input stimuli and absorption in CuMnAs serves as the sensor. Note that pulse widths of 150 fs are strongly exaggerated with respect to their time spacing of 700 ps for clarity in **f** (see the inset). **g**, Schematic depiction of a transient increase of effective CuMnAs temperature after absorption of the shown number of laser pulses; at room temperature (RT) the required temperature threshold ( $T_{TH}$ ) for achieving the switching is overpassed only for 8 and 16 pulses. **h**, Measured resistivity increase  $\Delta R$  in a device made from a 20-nm-thick CuMnAs epilayer, which shows that the number of rehearsals for information to be transferred from STM do LTM has to be at least 8 within the used 10-ns-long memorizing period. Laser pulses with a fluence of  $0.5 F_{TH}$  were used, where  $F_{TH}$  is a fluence needed to achieve the switching in a single-pulse experiment.

to a heat transfer from the GaP substrate to the sample holder and environment (see Fig. 3e), do not depend on the film thickness. Moreover, we have identified two additional characteristic (film-thickness-independent) time constants in STM dynamics on picosecond time scales:  $\tau_{ep} \sim 2.4$  ps, corresponding to electron-phonon relaxation time in CuMnAs (see Fig. 4e), and  $\tau_x \sim 20$  ps, whose origin is not certain at present (see Figs. 4c and 4d). Overall, this rich dynamic in STM on picosecond to sub-microsecond time ranges can serve as short-term synaptic plasticity [30,31] in the CuMnAs-based memory devices. Importantly, as we address later in the Discussion, we can mimic not only the pair-pulse facilitation (i.e., a transient synaptic strength increase) but also the pair-pulse depression (i.e., a synaptic strength decrease) features of the short-term synaptic behavior [30] in our devices.

In Fig. 2a we compare the cooling dynamics in 20-nm-thick and 50-nm-thick CuMnAs epilayers on (sub)nanosecond timescales. Clearly, due to the film-thickness-dependent time constant  $\tau_l$ , up to  $\sim 4$  ns this dynamics depends strongly on the film thickness. So, to demonstrate a tuneability of the STM-dynamics by the CuMnAs film thickness, without affecting the LTM-dynamics, we used 700 ps time spacing between laser pulses in the experiments depicted in Figs. 1 and 2. We note that changing the film thickness for a fixed pulse spacing affects STM in an analogous way as modulating the rehearsal frequency (see Fig. 1e) for a given CuMnAs film thickness. As shown in Fig. 2b, the required switching threshold is overpassed for 8 pulses for both film thicknesses. However, as in the 20 nm film the threshold is reached only barely, the resulting long-term resistive increase is much larger in the device made from the 50 nm film (but the LTM-dynamics is very similar in both cases), see Fig. 2c. Finally, we show that laser pulses can be used for a manipulation with stored information in LTM not only through STM. In Fig. 2d the dashed curve depicts the "forgetting" in LTM after 10 ns long memorizing period, when 16 rehearsals by laser pulses are performed to achieve the information transfer from STM to LTM. The solid line illustrates that laser pulses can significantly accelerate the LTM forgetting. In this case, laser pulses with the same intensity but with a much longer mutual time spacing than those used for the rehearsals (1 ms vs. 700 ps) started to be incident on the device at a certain moment, depicted as a vertical arrow in Fig. 2d. Alternatively, the same effect can be achieved by a single burst of laser pulses with a lowered intensity (see Fig. 4d in Ref. 12). In both cases, the mechanism responsible for this behavior is an accelerated resistance recovery when the device temperature is increased by the laser pulses, see Figs. 4a and 4b in Ref. 12.

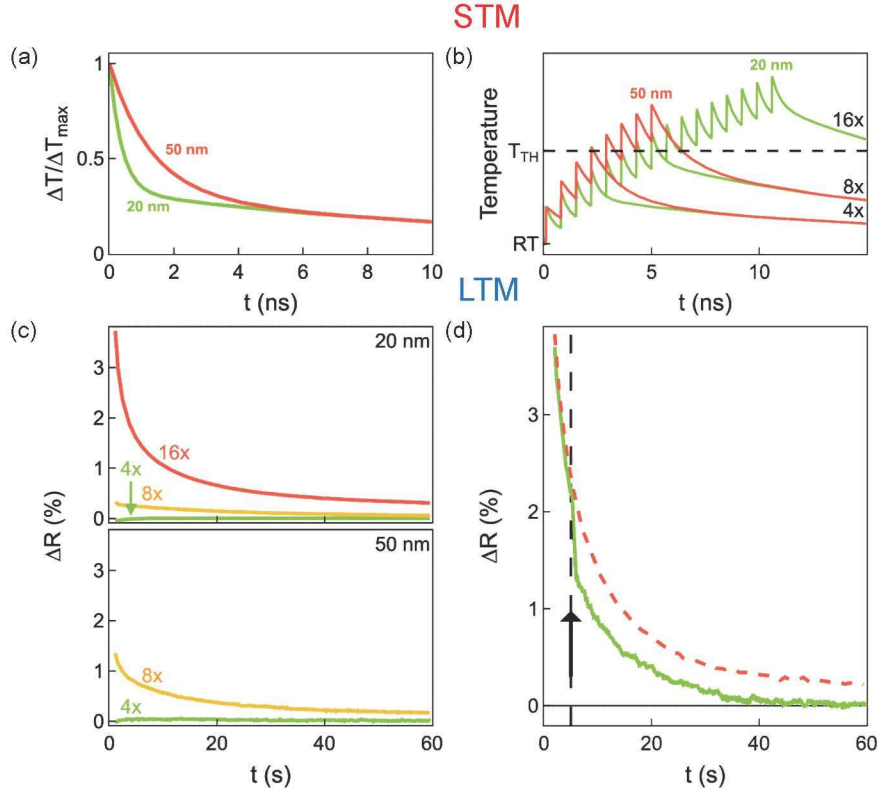


**Figure 2: Experimental demonstration of STM tuneability by the CuMnAs film thickness and a laser-induced erasing of memorized information in LTM.**

**a.** Cooling dynamics in CuMnAs films with thicknesses of 20 and 50 nm, as approximated by a sum of 3 exponential decay functions, see text for details. **b.** Schematic illustration of the transient temperature evolution in CuMnAs films with thicknesses of 20 and 50 nm after the impact of laser pulse bursts with a depicted number of femtosecond laser pulses with a time spacing of 700 ps (cf. Fig. 1e). At room temperature (RT) the required temperature threshold ( $T_{TH}$ ) for achieving the switching is overpassed for 8 pulses for both film thicknesses. However, as the threshold is reached only barely in the 20 nm film, the resulting long-term relative resistive increase is much larger in the device made from the 50 nm film, as shown in **c** for pulses with a fluence  $0.4 F_{TH}$ . **d.** Demonstration of a laser-induced erasing of information in LTM. The dashed curve shows the resistivity decay (i.e., a "forgetting" dynamics) measured after 10 ns long memorizing period, when 16 rehearsals by pulses with a fluence of  $0.4 F_{TH}$  and a time spacing of 700 ps in a device made from a 20-nm-thick film was used. The solid curve depicts that the forgetting can be significantly accelerated if at a certain moment (at 5 s in **d**, as indicated by a vertical arrow) laser pulses with the same fluence but much longer mutual time spacing of 1 ms start to be incident on the memory device.

### Separation of heat-related and switching-related signals in CuMnAs memory devices

In this section, we show how we experimentally separated the dynamics of heat-related (i.e., STM-like) and switching-related (LTM-like) resistance signals in our devices. As a first step, we performed a *single-pulse experiment* where the resistance change  $\Delta R$  induced by a single femtosecond-laser pulse is detected by a high-performance oscilloscope, as illustrated in Fig. 3a. The inset of Fig. 3b shows the two stretched-exponential relaxation components in  $\Delta R$  dynamics. The black rectangle highlights the temporal range dominated by the dynamics of the

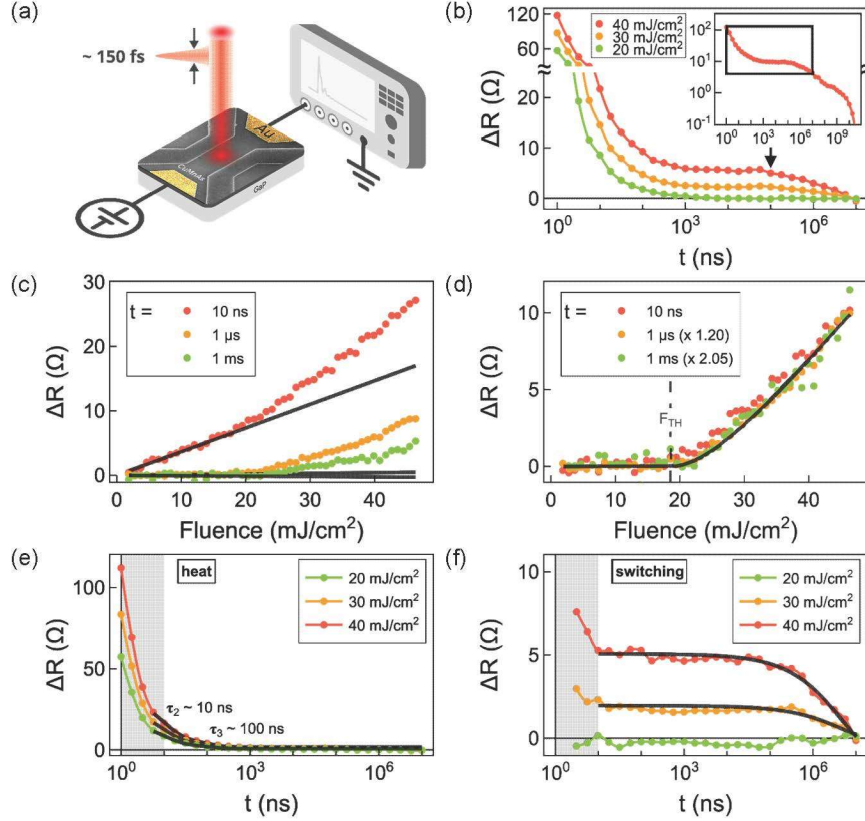


**Figure 3: Decomposition of measured device resistance change  $\Delta R$  into heating and switching contributions in a single-pulse experiment.**

**a**, Schematic illustration of the setup for optical excitation of a device using a single femtosecond laser pulse and for electrical readout of the resulting  $\Delta R$  by a fast oscilloscope. **b**, Stroboscopic optical-pump/electrical-probe measurements for three fluences of the pump laser pulse in a device made from a 20-nm-thick CuMnAs epilayer. The pulse-induced  $\Delta R$  as a function of the time  $t$  of the electrical probing are plotted relative to the device resistance at the end of the 10 ms measurement interval. Inset: Non-stroboscopic measurement of  $\Delta R$  relative to the equilibrium resistance, induced by a pump pulse with a fluence of 40 mJ/cm<sup>2</sup>, over an extended time interval. To improve the signal-to-noise ratio (see Methods), the stroboscopic experiments in the main panel were performed by illuminating the devices with a train of laser pulses at a repetition rate of 100 Hz, enabling measurements within a 10 ms interval, highlighted in the inset by the black rectangle. The black vertical arrow depicts the time where values of  $\Delta R$  shown in Figs. 4c and 4d were measured. **c**, As-measured fluence dependence of  $\Delta R$  at three distinct times  $t$  after the incidence of a single laser pulse (dots) in a device made from a 20-nm-thick CuMnAs epilayer. The heating contributions to the signals are depicted by solid lines. **d**, Same as **c** with the heating contributions subtracted; the obtained values (dots) for  $t = 1 \mu\text{s}$  and 1 ms are multiplied by the indicated factors to show the common fluence dependence. The line is a fit using a theoretical threshold model (see main text and Supplementary information, part B) that defines the value of the fluence threshold  $F_{TH}$ . **e**, **f**, Deduced time evolution of heating and switching contributions to  $\Delta R$ , respectively. Gray areas denote the time window where the applied decomposition method becomes unreliable (see Supplementary information, parts C and D, for a detailed discussion). The indicated heat relaxation time constants  $\tau_2$  and  $\tau_3$  were obtained by a double exponential fit (black solid lines) of experimental data in **e**. The relaxation of the switching signal (see Supplementary information, part C) in **f** is characterized by the Kohlrausch stretched-exponential model (lines).

faster-relaxing component on which we focus in the following systematic high-precision stroboscopic measurements. These are illustrated in the main panel of Fig. 3b for one laser fluence below the switching threshold and two above-threshold fluences. The pulse-induced  $\Delta R$  as a function of the electrical probing time  $t$  is plotted relative to the device resistance at the end of the



10 ms measurement interval. Fig. 3c shows the as-measured fluence-dependence of  $\Delta R$  at three distinct probing times  $t$  after the incidence of a single laser pulse. The linear dependence below the switching-threshold fluence corresponds to the heating contribution. The solid lines in Fig. 3c extrapolate the linear heating contribution to fluences above the switching threshold. In Fig. 3d we plot the fluence-dependence of  $\Delta R$  after subtracting the linear heating contribution. Data for  $t = 1 \mu\text{s}$  and  $1 \text{ ms}$  are multiplied by the indicated factors to highlight the universal switching-threshold characteristics. The line in Fig. 3d is a fit based on a model that considers the experimental Gaussian spatial profile of the laser beam, and describes the threshold fluence  $F_{TH}$  and the scaling of the switching contribution to  $\Delta R$  with the volume of the antiferromagnet excited above the switching threshold. (For more details see Supplementary information, part B.) Because of the Gaussian profile of the laser beam, we do not systematically explore the high-fluence regime corresponding to saturated  $\Delta R$  in our optical-pulsing experiments. In this regime, the excitation at the center of the laser beam exceeds the threshold for structurally damaging the antiferromagnetic crystal. In Figs. 3e and 3f we plot the  $t$ -dependence of the heating and switching contributions to  $\Delta R$ , respectively. They demonstrate that the heat and switching contributions to  $\Delta R$  can be reliably separated using our electrical probing method starting from  $\sim 10 \text{ ns}$  after the laser pulse. In this time range, the heat-related signals decay with time constants  $\tau_2 \sim 10 \text{ ns}$  and  $\tau_3 \sim 100 \text{ ns}$ , which we attribute to a heat transfer from the GaP substrate to the sample holder and environment. Importantly, the switching-related signals do not decay up to  $\sim 100 \mu\text{s}$ , when the fastest component in the Kohlrausch stretched-exponential model starts to be apparent (see Supplementary information, part C).

To study dynamics at (sub)picosecond timescales, we performed a *double-pulse experiment*, as illustrated in Fig. 4a. Here, the device is illuminated every 10 ms by a pair of laser pulses with an ultrashort mutual time delay  $\Delta t$  (see Fig. S5) and the resulting device resistance change is measured at macroscopic times  $t$ , typically at  $t \approx 0.1 \text{ ms}$ , after the incidence of the double-pulse. We choose a laser fluence such that one pulse alone would not cause switching, while for a simultaneous incidence of the two pulses ( $\Delta t = 0$ ) the combined fluence is safely above the switching threshold, see Fig. 4b. In Figs. 4c and 4d we compare measurements of  $\Delta R$ , detected at electrical probing time  $t = 0.1 \text{ ms}$ , as a function of the delay time  $\Delta t$  between the two successive pulses in devices fabricated from 20 nm and 50 nm thick CuMnAs epilayers. Initially, for  $\Delta t$  on a  $\sim \text{ps}$  timescale,  $\Delta R$  increases with increasing  $\Delta t$  (see the insets). This is then followed by decreasing  $\Delta R$  on  $\Delta t$ -scales of  $\sim 100 \text{ ps}$  in the 20 nm film and  $\sim 1000 \text{ ps}$  in the 50 nm film. A physical interpretation of the initial increase

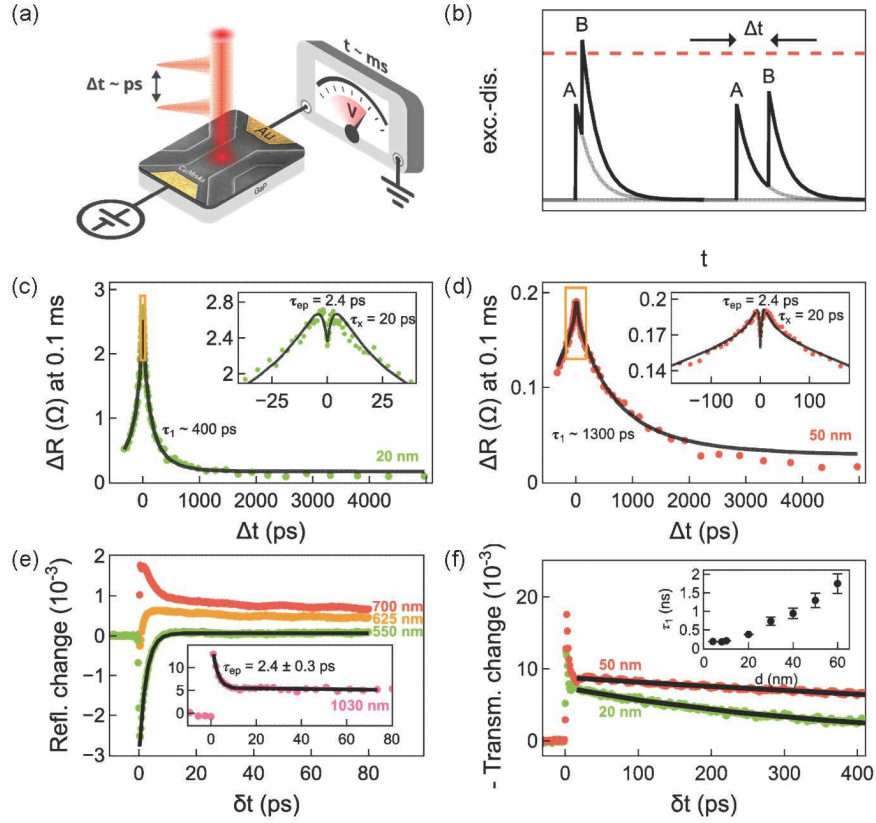


**Figure 4: Delay-time dependence of  $\Delta R$  in a double-pulse experiment.**

**a**, Schematic of the experimental setup for optical excitation of a device by a pair of laser pulses with a mutual ultrashort delay time  $\Delta t$ . The resulting change of the device resistance is measured at macroscopic times  $t$  after the incidence of the pair of laser pulses. **b**, Cartoon illustrating excitation of CuMnAs by the laser pulses followed by the energy dissipation. In the double-pulse experiments, the fluence of an individual pulse is not sufficient to excite the CuMnAs antiferromagnet over the switching threshold (red dashed line). **c**, Delay-time  $\Delta t$  dependence of  $\Delta R$  measured 0.1 ms after the incidence of the pair of laser pulses, which is indicated by a black vertical arrow in Fig. 3b, in a device made from a 20-nm-thick CuMnAs epilayer (dots). The solid line is a model described in the main text and Supplementary information, part E with electron-phonon relaxation time  $\tau_{ep}$ , time constant  $\tau_x$  and thermal-relaxation time  $\tau_l$  as fitting parameters. Inset: Detailed view of the data region near the zero-time overlap of the pulse pair, illustrated as a red rectangle in the main panel. **d**, Same as **c** for a device made from a 50-nm-thick CuMnAs epilayer. **e**, Dynamics of differential reflectivity  $dR/R$  in 50-nm-thick epilayer at 15 K for three selected wavelengths of probe pulses after excitation by 820 nm pump pulse with a fluence of 3 mJ.cm<sup>-2</sup> (dots). Inset: Dynamics of  $dR/R$  measured at 300 K using pump and probe pulses with a wavelength of 1030 nm and pump fluence of 20 mJ.cm<sup>-2</sup>. Lines are fits yielding the electron-phonon relaxation time  $\tau_{ep}$  (see main text and Supplementary information, part E for detailed discussion). **f**, Laser-pulse-induced dynamics of transient decrease of differential transmission  $dT/T$  measured by optical-pump/optical-probe experiment in 20-nm and 50-nm-thick CuMnAs epilayers at 15 K using pump and probe pulses with a wavelength of 820 nm (dots) and pump fluence of 3 mJ.cm<sup>-2</sup>. Lines are fits by a mono-exponential decay function with a characteristic time constant  $\tau_l$  corresponding to the heat dissipation from the CuMnAs epilayer to the GaP substrate. Inset: Dependence of  $\tau_l$  on the epilayer thickness.

of  $\Delta R$  is suggested by ultra-fast transient reflectivity measurements of CuMnAs, shown in Fig. 4e, which was obtained using a stroboscopic optical-pump/optical-probe method. In the inset of Fig. 4e, we show the optical-pump/optical-probe measurement using the same wavelength of pump and probe pulses as that in the double-pulse experiments in Figs. 4c and 4d, and using a sub-threshold

pump fluence. We observe that the pump pulse causes an abrupt increase of the reflectivity that decays with a characteristic time constant  $\tau_{ep} = 2.4 \pm 0.3$  ps. Based on the non-degenerate pump-probe measurements over a range of probe wavelengths shown in the main panel of Fig. 4e, we interpret [38,39,40] this time constant as an electron-phonon relaxation time in CuMnAs [41]. We, therefore, attribute the initial increase of  $\Delta R$  with increasing  $\Delta t$  on the  $\sim$  ps scale to an abrupt increase of the CuMnAs reflectivity caused by the first pulse, followed by a fast relaxation of the transiently enhanced reflectivity, which is influencing the switching efficiency of the second pulse. In Fig. 4f we show transient transmission measured using the optical-pump/optical-probe method over a larger range of pump-probe delays reaching several hundred ps. The transmission relaxation on these longer time scales reflects the heat dissipation from the CuMnAs film [41]. Consistently, the inferred thermal-relaxation time  $\tau_1$  increases with increasing film thickness, as highlighted in the inset of Fig. 4f. The change of  $\Delta R$  in the parts of the  $\Delta t$  dependencies in Figs. 4c and 4d, where  $\Delta R$  decreases with increasing  $\Delta t$ , is also on a considerably longer time scale in the 50 nm film than in the 20 nm film, and the overall scale is similar to  $\tau_1$  depicted in Fig. 4f. Qualitatively, we can therefore attribute the  $\sim 100 - 1000$  ps scale relaxation of  $\Delta R$  in Figs. 4c and 4d to the dissipation of the excitation energy delivered by the first pulse until the arrival of the second pulse. Finally, in contrast to the all-optical pump-probe experiments, where only time constants  $\tau_{ep}$  and  $\tau_1$  are apparent (see inset of Fig. 4e), an additional time constant  $\tau_x \sim 20$  ps is present in the measured decrease of  $\Delta R$  with  $\Delta t$ , as shown in insets of Figs. 4c and 4d. This time constant seems to be independent on the CuMnAs film thickness but its physical origin is not clear at this moment (see Supplementary information, parts D and E, for a detailed analysis and discussion of double-pulse experiments).

## DISCUSSION

In the remaining paragraphs, we discuss our experimental results in a broader context of the research of compensated magnets towards ultra-scalable analog logic-in-memory devices and neuromorphic computing. Earlier experimental works have focused on spiking neuromorphic functionalities in antiferromagnetic devices operated down to  $\sim 10$  ns time scales [42]. Our work demonstrates a concept capable of dealing with spikes of length on the sub-ps scale and delay times down to the ps range using an elementary resistor-geometry device. Our results also open the route for a development of artificial synapses with spike-timing-dependent plasticity [30,42] at the ultra-short ps-time scales, where the functionality is based on the changing value of the encoded variable resistance of the analog memory with increasing delay time between successive spikes. In recent

years, artificial synaptic devices have attracted considerable interest [35,43-46] due to their great potential to serve as building blocks for non-von Neumann neuromorphic computing. However, at the system level of bio-inspired neural networks, only the long-term synaptic plasticity is used at present [47-50] while emulation of short-term synaptic plasticity (STP) is still limited to the device level [30,31]. In a biological synapse, STP is associated with a neurotransmitter release, which is connected with a (rather complex) kinetics of intracellular calcium concentration [30,31]. In artificial synapses, STP is typically achieved by a device conductance control by external means (see Ref. 30 for a detailed review about reported STP-based devices). In previous studies of STM to LTM transition in artificial synaptic devices, both electrical [33-35,51-53] and optical [54-59] pulses were used. However, in all these preceding studies the used pulse durations were in milliseconds to seconds time ranges. In our case, we are using laser pulse bursts consisting of femtosecond laser pulses with a picosecond to nanosecond mutual time spacing that is time-matched to the ultrafast reflectivity change or heat dissipation from nanometer-thin CuMnAs films, which serve as ultrafast STM. An upper estimate of  $\sim 10$  ps for the time needed to achieve the information transfer from STM to LTM can be deduced from the double-pulse experiments (see Supplementary information, Part F).

In this study, we use light pulses as ultrashort input stimuli for our devices. The main reason is that the generation of femtosecond laser pulses is a mature technology readily available in commercial table-top laser systems. However, light is not the only stimulus compatible with our devices. As metals are absorbing in a broad frequency range, THz pulses [11], short electrical pulses [12], and/or their combinations with optical pulses can be also used to achieve the CuMnAs switching. This feature might be rather important for achieving a mutual communication between individual devices, as demonstrated in a spintronic neural network constructed from nano-oscillators, where radiofrequency signals were used for this purpose [60]. In CuMnAs-based devices, the required energy-per-pulse for achieving the switching is primarily determined by the device size, i.e., by the switched volume of the antiferromagnet (see Supplementary Fig. S2). In this paper, we used predominantly microbar devices with dimensions  $10 \times 20 \mu\text{m}^2$  illuminated by Gaussian spatial-profile laser pulses with a diameter of  $20 \mu\text{m}$ , where the switching threshold fluence corresponds to 36 nJ of delivered energy per pulse (see Supplementary information, part B). For smaller devices (illuminated by more tightly focused laser beams) the required energy is considerably smaller. Due to technical limitations, we are not able to prepare devices with sizes below  $\sim 1 \mu\text{m}^2$ , where the switching threshold energy reaches  $\sim 100$  pJ [61]. Considering the recent

discovery of atomically-sharp domain walls in CuMnAs antiferromagnet [36], it is reasonable to expect that the device size could be potentially scaled down to  $\sim$  nm dimensions. At this limit, assuming a CuMnAs device with a volume of  $10 \text{ nm}^3$ , the switching energy would be  $\sim 3.5 \text{ fJ}$ , which is comparable to the  $\sim 1\text{-}100 \text{ fJ}$  per synaptic event in biological systems [62].

As a last remark, we would like to mention that, apart from the ultrashort duration and experimental availability, laser pulses possess another appealing feature for the proof-of-principle demonstrations of artificial synaptic devices based on antiferromagnetic metals switching. As the pump-induced transient optical response (reflection and absorption) of metals depends on the wavelength of the used laser pulses (see Fig. 4e), it also affects the short-term synaptic behavior in these devices. In the double-pulse experiment with all pulses at  $1030 \text{ nm}$ , we observed "dips" in the dependence of  $\Delta R$  on  $\Delta t$  (see insets of Figs. 4c and 4d) due to an abrupt increase of the CuMnAs reflectivity caused by the first pulse, which is influencing the switching efficiency of the second pulse. This "reduced sensitivity" to the second pulse is analogous to the pair-pulse depression (i.e., a transient synaptic strength decrease due to the neurotransmitter depletion) in a biological synapse [30]. If the second laser pulse wavelength were  $550 \text{ nm}$ , for example, we would obtain an "enhanced sensitivity" to the second pulse due to a transient reflectivity reduction (see Fig. 4e), i.e., the pair-pulse facilitation (i.e., a transient synaptic strength increase) instead. Overall, the possibility to modify the device performance by the CuMnAs film thickness, device temperature, and laser pulse wavelength opens a rich playground for a functionality optimization of these analog STM/LTM devices.

## ONLINE METHODS

### Samples

Tetragonal CuMnAs epilayers were grown using molecular beam epitaxy on lattice-matched GaP substrate at temperatures around  $200^\circ\text{C}$ . The films were capped with a  $3 \text{ nm}$  Al layer, which quickly oxidized after removal from the vacuum, preventing oxidation of the CuMnAs. Microbar devices (Fig. 1d and Fig. 3a) with typical dimensions of  $10 \times 20 \mu\text{m}^2$  were lithographically patterned from 20- or 50-nm-thick epilayers (with a sheet resistance of 50 and  $20 \Omega$ , respectively). Electron-beam lithography and wet chemical etching were used to pattern the majority of studied devices. The aluminum cap was removed in 2.7%  $\text{C}_4\text{H}_{13}\text{NO}$  (for 3 s) and a mixture of  $\text{H}_3\text{PO}_4\text{:H}_2\text{O}_2\text{:H}_2\text{O}$  in ratio 1:10:400 was used as the CuMnAs etchant, providing an etching rate of  $50 \text{ nm}$  per  $20 \text{ s}$ . A custom-designed, two-terminal high-frequency printed circuit

board sample holder was employed for bonding gold contacts sputtered onto the opposing ends of the microbars. Long-term resistive experiments (shown in Figs. 2c and 2d) were performed on four-terminal devices with typical dimensions of  $20 \times 20 \mu\text{m}^2$ , optimized for four-point resistance measurements. In this case, UV-lithography was utilized for patterning the devices and an alkaline developer was employed to remove the aluminum capping layer during the resist development phase.

### **Measurement of device resistance changes after impact of a burst of equiamplitude and equidistant femtosecond laser pulses**

An Yb-based femtosecond laser system (Pharos, Light Conversion) is used as the light source for optical writing. This laser can produce a single laser pulse with a 150 fs pulse duration and a central wavelength of 1030 nm, utilizing the controlling software pulse-on-demand functionality. The single laser pulse is split into  $N$  mutually identical copies, separated by equidistant time delays  $\Delta t = 700$  ps, using a pulse-multiplier experimental setup, as shown in Figs. S1c to S1f in Supplementary information, part A. In our experiment, each laser pulse burst contains  $N = 1, 2, 4, 8$ , or 16 laser pulses with a computer-controlled laser fluence. The pulses are focused onto a single spot on the sample, exhibiting a Gaussian intensity profile with a diameter of  $20 \mu\text{m}$  (see Supplementary information, part A), to excite the studied devices. A four-point measurement configuration (utilizing a Keithley 6500 multimeter and a Keithley 2400 sourcemeter with  $100 \mu\text{A}$  probing current) is used to record the laser-induced change in the device resistance in a real-time domain every 0.1 s for 60 s following the burst incidence. For a given laser pulse fluence and a selected number of  $N$  pulses in a burst, three acquisitions are typically measured and averaged to enhance data quality. All measurements are performed at room temperature.

### **Stroboscopic experiment combining optical writing and electrical readout**

In this experiment, an Yb-based femtosecond laser system (Pharos, Light Conversion) is used as the light source. Laser pulses, with a 150 fs pulse duration, a central wavelength of 1030 nm, and a user-selectable repetition rate, are divided into two branches with a precise control of their mutual time delay (see Supplementary Fig. S1a). The laser pulses were focused onto a single spot on the sample, exhibiting a Gaussian intensity profile with a diameter of  $20 \mu\text{m}$  (see

Supplementary information, part A). The fluence of laser pulses in each branch is independently controlled by a computer, enabling fluences up to 50 mJ/cm<sup>2</sup>.

Time-resolved electrical readout is performed using a Rohde & Schwarz RTP064 high-performance oscilloscope, with a 6 GHz bandwidth, while a Rigol DG1000Z serve as the voltage source. The electrical setup schematic is illustrated in Supplementary Fig. S1b. Voltage measurements are taken across the input resistance of the oscilloscope, which is connected in series with the sample. The sample's resistance is deduced from these voltage readings (see Supplementary information, part A), and the resistance increase, relative to the device resistance at the end of the measurement time window, is computed. Typically, 2.5 million data points are collected during a single acquisition of the selected measurement range. To reduce noise at high frequencies without compromising the time resolution, the majority of experiments is performed with the laser operating at a 100 Hz repetition rate, corresponding to 10 ms time-spacing between adjacent laser pulses, and  $\approx 100$  acquisitions are averaged for each measurement. Consequently, only time transients faster than 10 ms are apparent in the measured data (see Fig. 3b). All measurements are performed at room temperature.

Using this experimental setup, two types of experiments can be performed, which are shown schematically in Figs. 3a and 4a, respectively. In the first type, the sample is illuminated by a single laser pulse every 10 ms and the oscilloscope records the corresponding resistance changes within this window. Here, the time variable  $t$  represents the oscilloscope measurement time, with  $t = 0$  ns defined as the time when the measured waveform reaches its maximum (see Fig. S5a). The overall time resolution of this oscilloscope measurement corresponds to the  $\approx 2$  ns electrical signal rise time after the femtosecond laser pulse impact, which is depicted as a gray area in Fig. S5a. In the second type, the sample is illuminated every 10 ms by a pair of laser pulses with an ultrashort mutual time delay  $\Delta t$  (see Fig. S5) and the resulting device resistance change is measured at macroscopic times  $t$ , typically at  $t \approx 0.1$  ms, after the incidence of the double-pulse. The time-zero delay,  $\Delta t = 0$  ps, corresponds to a simultaneous incidence of both laser pulses on the device. Importantly, this second type of experiment provides a much better time resolution, which is primarily determined by the time-width of the used laser pulses of  $\approx 150$  fs.

### **Pump-probe experiment**

We performed both a degenerate pump-probe experiment, where the same wavelength of pump and probe pulses is used, and also its non-degenerate variety, with a non-equal wavelength

of pump and probe pulses. For the degenerate pump-probe experiment at 1030 nm, we used the Yb-based femtosecond laser system with the experimental parameters described above. In addition, a degenerate pump-probe experiment at 820 nm was performed using a femtosecond Ti:Sapphire oscillator (Mai Tai, Spectra Physics) generating  $\approx 150$  fs laser pulses at a repetition rate of 80 MHz – see Fig. 1a in Ref. 63 for the corresponding experimental setup.

For the non-degenerate pump-probe experiment we used the fundamental output from the Ti:Sapphire oscillator at 820 nm as a pump beam and the output from an optical parametric oscillator (Inspire, Spectra Physics), tunable from 550 nm to 700 nm, as a probe beam. The pulses are focused onto the same spot on the sample (with a Gaussian diameter of  $\approx 35$   $\mu\text{m}$ ) at nearly normal incidence (see Supplementary information, part A). The laser fluence of the pump pulses is approximately 3 mJ/cm<sup>2</sup> (i.e., well below the CuMnAs switching threshold), while the probe pulses are at least 50 times weaker. The experiment is performed at temperature of 15 K. Here, we simultaneously measure the pump-induced transient changes of CuMnAs transmission (the differential transmission  $dT/T = (T_E - T)/T$ , where  $T_E$  and  $T$  are transmissions with and without the pump pulse, respectively) and reflectivity (differential reflectivity  $dR/R = (R_E - R)/R$ , where  $R_E$  and  $R$  are reflectivities with and without the pump pulse, respectively). For more details, see Ref. 41.

## REFERENCES

- [1] Němec, P., Fiebig, M., Kampfrath, T. & Kimel, A. V. Antiferromagnetic optospintronics. *Nature Physics* **14**, 229–241 (2018).
- [2] Landauer, R. Irreversibility and Heat Generation in the Computing Process. *IBM Journal of Research and Development* **5**, 183–191 (1961).
- [3] Kimel, A. V., Kalashnikova, A. M., Pogrebna, A. & Zvezdin, A. K. Fundamentals and perspectives of ultrafast photoferroic recording. *Physics Reports* **852**, 1–46 (2020).
- [4] Schlauderer, S. *et al.* Temporal and spectral fingerprints of ultrafast all-coherent spin switching. *Nature* **569**, 383–387 (2019).
- [5] Železný, J. *et al.* Relativistic Néel-order fields induced by electrical current in antiferromagnets. *Physical Review Letters* **113**, 157201 (2014).
- [6] Wadley, P. *et al.* Electrical switching of an antiferromagnet. *Science* **351**, 587–590 (2016).
- [7] Wadley, P. *et al.* Current polarity-dependent manipulation of antiferromagnetic domains. *Nature Nanotechnology* **13**, 362–365 (2018).



- [8] Behovits, Y. *et al.* Nonlinear terahertz Néel spin-orbit torques in antiferromagnetic Mn<sub>2</sub>Au (2023). *Nat. Commun.* **14**, 146038 (2023).
- [9] Fukami, S., Zhang, C., Duttagupta, S., Kurenkov, A. & Ohno, H. Magnetization switching by spin-orbit torque in an antiferromagnet-ferromagnet bilayer system. *Nature Materials* **15**, 535–541 (2016).
- [10] Olejník, K. *et al.* Antiferromagnetic CuMnAs multi-level memory cell with microelectronic compatibility. *Nature Communications* **8**, 15434 (2017).
- [11] Olejník, K. *et al.* Terahertz electrical writing speed in an antiferromagnetic memory. *Science Advances* **4**, eaar3566 (2018).
- [12] Kašpar, Z. *et al.* Quenching of an antiferromagnet into high resistivity states using electrical or ultrashort optical pulses. *Nature Electronics* **4**, 30–37 (2021).
- [13] Jungwirth, T., Marti, X., Wadley, P. & Wunderlich, J. Antiferromagnetic spintronics. *Nat. Nanotech.* **11**, 231–241 (2016).
- [14] Baltz, V. *et al.* Antiferromagnetic spintronics. *Rev. Mod. Phys.* **90**, 015005 (2018).
- [15] Kurenkov, A., Fukami, S. & Ohno, H. Neuromorphic computing with antiferromagnetic spintronics. *J. Appl. Phys.* **128**, 010902 (2020).
- [16] Zhang, S. & Tserkovnyak, Y. Antiferromagnet-based neuromorphics using dynamics of topological charges. *Phys. Rev. Lett.* **125**, 207202 (2020).
- [17] Bindal, N., Ian, C. A. C., Lew, W. S. & Kaushik, B. K. Antiferromagnetic skyrmion repulsion based artificial neuron device. *Nanotechnology* **32**, 215204 (2021).
- [18] Brehm, V., Austefjord, J.W., Lepadatu, S. & Qaiumzadeh, A. A proposal for leaky integrate-and-fire neurons by domain walls in antiferromagnetic insulators. *Sci. Rep.* **13**, 13404 (2023).
- [19] Bradley, H. *et al.* Artificial neurons based on antiferromagnetic auto-oscillators as a platform for neuromorphic computing. *AIP Advances* **13**, 015206 (2023).
- [20] Drachman, D. A. Do we have brain to spare? *Neurology* **64**, 2004–2005 (2005).
- [21] Yang, J. T. *et al.* Artificial synapses emulated by an electrolyte-gated tungsten-oxide transistor. *Adv. Mater.* **30**, 1801548 (2018).
- [22] Fuster, J.M., & Alexander, G.E. Neuron activity related to short-term memory. *Science* **173**, 652–654 (1971).
- [23] Abbott, L.F., & Regehr, W.G. Synaptic computation. *Nature* **431**, 796–803 (2004).
- [24] Zucker, R.S., & Regehr, W.G., Short-term synaptic plasticity. *Annu. Rev. Physiol.* **64**, 355–405 (2002).

- [25] Grande, L.A., & Spain, W.J., Synaptic depression as a timing device. *Physiology* **20**, 201–210 (2005).
- [26] Regehr, W.G., Short-term presynaptic plasticity. *Cold Spring Harbor Perspect. Biol.* **4**, a005702 (2012).
- [27] Shiffrin, R.M., & Atkinson, R.C. Storage and retrieval processes in long-term memory. *Psychol. Rev.* **76**, 179–193 (1969).
- [28] Bliss, T.V., & Collingridge, G.L. A synaptic model of memory: long-term potentiation in the hippocampus. *Nature* **361**, 31–39 (1993).
- [29] Bi, G., & Poo, M., Synaptic modification by correlated activity: hebb’s postulate revisited. *Annu. Rev. Neurosci.* **24**, 139–166 (2001).
- [30] Li, Ch., Zhang, X., Chen, P., Zhou, K., Yu, J., Wu, G., Xiang, D., Jiang, H., Wang, M., & Liu Q., Short-term synaptic plasticity in emerging devices for neuromorphic computing. *iScience* **26**, 106315 (2023).
- [31] Hennig, M.H., Theoretical models of synaptic short term plasticity. *Front. Comput. Neurosci.* **7**, 45 (2013).
- [32] Atkinson, R. C. & Shiffrin, R. M. in *The Psychology of Learning and Motivation: Advances in Research and Theory* Vol. 2 (eds Spence, K. W. & Spence, J. T.) 89-195 (Academic, 1968).
- [33] Ohno, T. *et al.* Short-term plasticity and long-term potentiation mimicked in single inorganic synapses. *Nat. Mater.* **10**, 591–595 (2011).
- [34] Chang T., Jo S.H. & Lu W, Short-term memory to long-term memory transition in a nanoscale memristor. *ACS Nano* **5**, 7669–7676 (2011).
- [35] Ji, X., Paulsen, B.D., Chik, G.K.K., Wu, R., Yin, Y., Chan, P.K.L., & Rivnay, J. Mimicking associative learning using an ion-trapping non-volatile synaptic organic electrochemical transistor. *Nat. Commun.* **12**, 2480 (2021).
- [36] Křížek, F. *et al.* Atomically sharp domain walls in an antiferromagnet. *Science Advances* **8**, eabn3535 (2022).
- [37] Křížek, F. *et al.* Molecular beam epitaxy of CuMnAs. *Physical Review Materials* **4**, 014409 (2020).
- [38] Sun, C.-K., Vallée, F., Acioli, L. H., Ippen, E. P., & Fujimoto, J. G. Femtosecond-tunable measurement of electron thermalization in gold. *Phys. Rev. B* **50**, 15337 (1994).

- [39] Djordjevic, M., Lüttich, M., Moschkau, P., Guderian, P., Kampfrath, T., Ulbrich, R. G., Münzenberg, M., Felsch, W. & Moodera, J. S. Comprehensive view on ultrafast dynamics of ferromagnetic films. *Phys. Status Solidi C* **3**, 1347 (2006).
- [40] Carpena, E., Mancini, E., Dallera, C., Brenna, M., Puppini, E. & Silvestri, S. D., Dynamics of electron-magnon interaction and ultrafast demagnetization in thin iron films. *Phys. Rev. B* **78**, 174422 (2008).
- [41] Surýnek, M., Saidl, V., Novák, V., Campion, R.P., Wadley, P., & Němec, P. Investigation of magnetic anisotropy and heat dissipation in thin films of compensated antiferromagnet CuMnAs by pump–probe experiment. *J. Appl. Phys.* **127**, 233904 (2020).
- [42] Kurenkov, A. *et al.* Artificial Neuron and Synapse Realized in an Antiferromagnet/Ferromagnet Heterostructure Using Dynamics of Spin–Orbit Torque Switching. *Advanced Materials* **31**, 1900636 (2019).
- [43] Kuzum, D., Yu, S., & Wong, H. P. Synaptic electronics: materials, devices and applications. *Nanotechnology* **24**, 382001 (2013).
- [44] Wang, Z. *et al.* Nanoionics-enabled memristive devices: strategies and materials for neuromorphic applications. *Adv. Electron. Mater.* **3**, 1600510 (2017).
- [45] He, Y., Yang, Y., Nie, S., Liu, R. & Wan, Q. Electric-double-layer transistors for synaptic devices and neuromorphic systems. *J. Mater. Chem. C* **6**, 5336–5352 (2018).
- [46] Van De Burgt, Y., Melianas, A., Keene, S. T., Malliaras, G., & Salleo, A. Organic electronics for neuromorphic computing. *Nat. Electron.* **1**, 386–397 (2018).
- [47] Jeong, D.S., Kim, I., Ziegler, M., & Kohlstedt, H. Towards artificial neurons and synapses: a materials point of view. *RSC Adv.* **3**, 3169–3183 (2013).
- [48] Burr, G.W. *et al.* Neuromorphic computing using nonvolatile memory. *Adv. Phys. X* **2**, 89–124 (2017).
- [49] Wan, Q., Sharbati, M.T., Erickson, J.R., Du, Y., & Xiong, F., Emerging artificial synaptic devices for neuromorphic computing. *Adv. Mater. Technol.* **4**, 1900037 (2019).
- [50] Wang, J., & Zhuge, F., Memristive synapses for brain-inspired computing. *Adv. Mater. Technol.* **4**, 1800544 (2019).
- [51] Yang R., Terabe K., Liu G., Tsuruoka T., Hasegawa T., Gimzewski J.K., & Aono M. On-demand nanodevice with electrical and neuromorphic multifunction realized by local ion migration. *ACS Nano* **6**, 9515–9521 (2012).

- [52] Abbas, H. *et al.*, The coexistence of threshold and memory switching characteristics of ALD HfO<sub>2</sub> memristor synaptic arrays for energy-efficient neuromorphic computing. *Nanoscale* **12**, 14120–14134 (2020).
- [53] He, N. *et al.*, Multifunctional Ag–In–Zn–S/Cs<sub>3</sub>Cu<sub>2</sub>Cl<sub>5</sub>-Based Memristors with Coexistence of Non-Volatile Memory and Volatile Threshold Switching Behaviors for Neuroinspired Computing. *Adv. Electron. Mater.* **9**, 2201038 (2023).
- [54] Lin, T.R., Shih, L.C., Cheng, P.J., Chen, K.T., & Chen, J.S. Violet-light stimulated synaptic and learning functions in a zinc–tin oxide photoelectric transistor for neuromorphic computation. *RSC Adv.* **10**, 42682–42687 (2020).
- [55] Zhao, Y., Feng, G., & Jiang J. Poly(vinyl alcohol)-gated junctionless Al-Zn-O phototransistor for photonic and electric hybrid neuromorphic computation. *Solid State Electronics* **165**, 107 (2020).
- [56] Hao, D., Liu, D., Zhang, J., Wang, Y., & Huang, J. Lead-Free Perovskites-Based Photonic Synaptic Devices with Logic Functions. *Adv. Mater. Technol.* **6**, 2100678 (2021).
- [57] Li, N. *et al.*, Gate-Tunable Large-Scale Flexible Monolayer MoS<sub>2</sub> Devices for Photodetectors and Optoelectronic Synapses. *Nano Research* **15**, 5418 (2022).
- [58] Dong, L. *et al.*, Artificial Optoelectronic Synapse Based on Violet Phosphorus Microfiber Arrays. *Small* **23**, 2306998 (2023).
- [59] Zhao, P. *et al.*, Self-powered optoelectronic artificial synapses based on a lead-free perovskite film for artificial visual perception systems. *J. Mater. Chem. C* **11**, 6212–6219 (2023).
- [60] Ross, A. *et al.* Multilayer spintronic neural networks with radiofrequency connections, *Nat. Nanotechnol.* **18**, 1273–1280 (2023).
- [61] Zubáč, J., Surýnek, M. *et al.*, to be published.
- [62] van de Burgt, Y. *et al.*, A non-volatile organic electrochemical device as a low-voltage artificial synapse for neuromorphic computing. *Nature Materials* **16**, 414 (2017).
- [63] Surýnek, M., Nádvorník, L., Schmoranzarová, E. & Němec, P. Quasi-nondegenerate pump-probe magneto-optical experiment in GaAs/AlGaAs heterostructure based on spectral filtration. *New J. Phys.* **22**, 093065 (2020).

## Acknowledgements

The authors acknowledge funding by the Czech Science Foundation through projects GACR (grants no. 19-28375X and 21-28876J), the Grant Agency of the Charles University (grants no. 166123 and

SVV–2023–260720)), by CzechNanoLab Research Infrastructure supported by MEYS CR (LM2023051), and by MEYS CR project LNSM-LNSpin.

#### **Author contributions**

P.N., K.O., M.S., J.Z., L.N., and T.J. planned the experiments, J.Z., A.F., V.N. and F.K. prepared the samples, M.S., J.Z. and F.T. prepared the software for the data acquisition, M.S., J.Z., A.F., and P.K. performed the experiments, T.J., M.S. and P.N. wrote the manuscript with contributions from all authors.

#### **Additional information**

Supplementary information is available in the online version of the paper. Correspondence and requests for materials should be addressed to P.N.

#### **Competing financial interests**

The authors declare no competing financial interests.

# **Picosecond transfer from short-term to long-term memory in analog antiferromagnetic memory device: Supplementary information**

M. Surýnek<sup>1</sup>, J. Zubáč<sup>2,1</sup>, K. Olejník<sup>2</sup>, A. Farkaš<sup>2,1</sup>, F. Křížek<sup>2</sup>, L. Nádvorník<sup>1</sup>, P. Kubaščík<sup>1</sup>,  
F. Trojánek<sup>1</sup>, R.P. Campion<sup>3</sup>, V. Novák<sup>2</sup>, T. Jungwirth<sup>2,3</sup>, and P. Němec<sup>1</sup>

<sup>1</sup>Faculty of Mathematics and Physics, Charles University, Ke Karlovu 3, 121 16 Prague 2,  
Czech Republic

<sup>2</sup>Institute of Physics ASCR, v.v.i., Cukrovarnická 10, 162 53 Prague 6, Czech Republic

<sup>3</sup>School of Physics and Astronomy, University of Nottingham, Nottingham NG7 2RD,  
United Kingdom

## **CONTENTS**

A. Experimental details .....	2
B. Switching threshold model and effect of local resistivity change on device resistance .....	5
B1. Switching threshold model .....	5
B2. Estimation of threshold switching energy .....	7
B3. Effect of local resistivity change on device resistance .....	7
C. Single-pulse method: Separation of switching and heat contributions from measured resistance change .....	8
D. Double-pulse method: Heat accumulation and separation of signals for two mutually-time-delayed pulses .....	11
E. Heat dissipation dynamics .....	16
E1. Effective switching fluence in the double pulse experiment .....	16
E2. Heat dynamics model .....	18
F. Speed limit estimation for STM to LTM information transfer .....	22
References .....	22

## A. Experimental details

The stroboscopic optical writing experiments were performed using an Yb-based femtosecond laser system (Pharos, Light Conversion). As shown in Fig. S1a, laser pulses, with a pulse duration of 150 fs, a central wavelength of 1030 nm, and a user-tunable repetition rate, were split into two optical paths via a polarizing beam splitter (PBS), where their intensity was independently regulated by a pair of computer-controlled half-waveplates ( $\lambda/2$ ). The laser pulses were subsequently focused into a single spot on the sample, producing a Gaussian intensity profile

$$I(r) = I_0 \cdot e^{-\frac{r^2}{w^2}} \quad (S.A1)$$

where  $r$  is the radial distance from the center of the Gaussian profile. The experimentally achieved beam size, characterized by a full-width  $2w \approx 20 \mu\text{m}$ , was determined using the knife-edge method.

The corresponding time-resolved electrical measurements were carried out using a Rohde & Schwarz RTP064 high-performance oscilloscope with a bandwidth of 6 GHz for readout and a Rigol DG1000Z as a voltage source ( $U_{\text{source}} = 150 \text{ mV}$ ,  $R_{\text{source}} = 50 \Omega$ ). The schematic of the electrical setup is presented in Fig S1b. We recorded the voltage  $U$  across the input resistance  $R_{\text{scope}} = 50 \Omega$  of the oscilloscope, connected in series with the sample. The resistance of the sample was then determined by

$$R = \frac{U_{\text{source}} * R_{\text{scope}}}{U} - R_{\text{source}} - R_{\text{scope}} \quad (S.A2)$$

Subsequently, we corrected  $R$  by applying the oscilloscope's attenuation factor (in our case  $\text{atten} = 1 \text{ dB}$ ):

$$R_{\text{sample}} = R / \sqrt{10^{\text{atten}[\text{dB}]/10}} \quad (S.A3)$$

Typically, we collected 2.5 M data points during a single acquisition over a 10  $\mu\text{s}$  or 10 ms measurement range, corresponding to the laser's duty cycle. To minimize noise at high frequencies without compromising time resolution, we generally averaged curves from approximately 100 acquisitions.

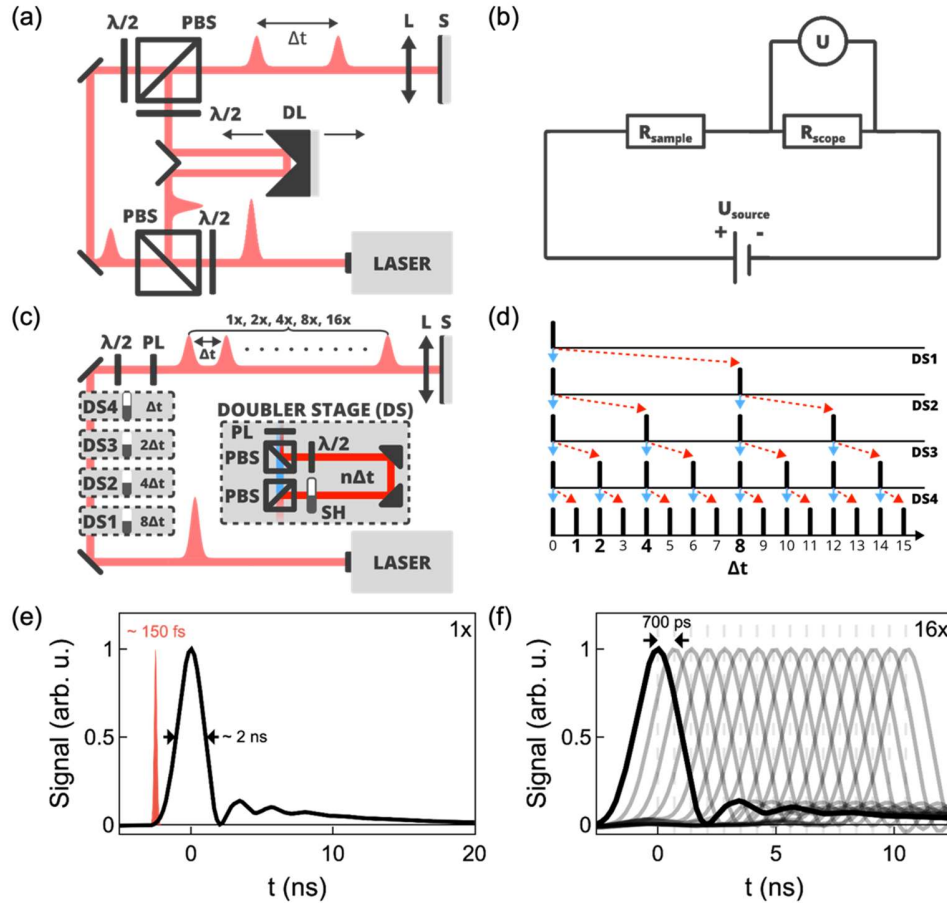


**Fig. S1 | Experimental setups used for optical switching measurements with electrical readout.** **a**, Optical setup for stroboscopic experiments: A beam generated by a femtosecond laser system is split into two paths by a polarizing beam splitter (PBS) and independent intensity control in each path is achieved with half-wave plates ( $\lambda/2$ ). An optical delay line (DL) adjusts the mutual time delay ( $\Delta t$ ) between laser pulses in the paths, which are spatially recombined by a second PBS and focused onto the sample (S) using a lens (L). **b**, Electrical readout setup for stroboscopic experiments. **c**, Pulse-multiplier setup. A laser pulse is divided into up to 16 equiamplitude and equidistant  $\Delta t$ -delayed pulses by passing through doubler stages DS1-DS4, each of them inducing the indicated time delay, which form the pulse burst incident on the sample. Grey rectangle: An individual doubler stage (DS) where a diagonally polarized laser pulse is split and consequently spatially recombined by a pair of PBS. Here, a delay line introduces a mutual time delay  $n\Delta t$  between the transmitted (blue path, horizontal polarization) and reflected pulse (red path, vertical polarization). A computer-controlled shutter (SH) allows to block the reflected pulse. A half-wave plate or a polarizer (PL) changes the polarization of both pulses to a diagonal one allowing a serial chaining of the stages. **d**, A cartoon depicting a single laser pulse splitting across doubler stages DS1-DS4. Blue solid arrows indicate transmitted pulses and red dashed arrows correspond to reflected pulses, which can be either blocked (state 0) or allowed to pass (state 1) by the shutter SH in each DS. **e**, Time-resolved signal measured by an avalanche photodiode (black) after impact of one 150-fs-long laser pulse (red). **f**, Normalized signals for 16 individual laser pulses from the burst, which are mutually time delayed for  $\Delta t = 700$  ps.



Besides stroboscopic optical writing experiments described above, we also investigated device resistance changes after the impact of a burst of laser pulses. For that we constructed a pulse-multiplier setup shown in Fig. S1c. This setup divides a single laser pulse, generated by our femtosecond laser system with a pulse-on-demand functionality, into  $N$  nearly identical copies, producing a burst of 1, 2, 4, 8, or 16 laser pulses with equidistant time delays  $\Delta t$ . A key component in this setup is a doubler stage (DS in Fig. S1c). Here, an incoming laser pulse with a diagonal polarization is split by a polarization beam splitter (PBS) into two pulses: the transmitted horizontally polarized pulse (blue in Fig. S1c) and the reflected vertically polarized pulse (red). The reflected pulse is either blocked (state 0) by a computer-controlled shutter (SH) or is allowed to pass (state 1) through a delay line to acquire a specific time delay ( $n\Delta t$ ) relative to the transmitted pulse. Next, the second PBS recombines both optical beams. In the constructed setup, as the intensity of reflected pulse is slightly higher compared to the transmitted one, a half-wave plate ( $\lambda/2$ ) in the reflected pulse branch is used to equalize the intensities of pulses from each branch after the second PBS. Finally, a half-wave plate or a polarizer (PL) is used to make a diagonal polarization of both pulses, which allows for a serial chaining of several DS units. In particular, stages DS1-DS4 with delay lines producing from  $8\Delta t$  to  $\Delta t$  were employed to generate bursts of up to 16 laser pulses from a single input pulse. After the pulse-multiplier, a half-wave plate ( $\lambda/2$ ) followed by a PL was used to regulate the burst intensity. Analogous to the setup in Fig. S1a, the laser pulse burst was eventually focused onto a single spot on the sample.

Fig. S1d illustrates the laser pulses propagation and splitting across the individual doubler stages. Solid blue arrows indicate transmitted pulses, while red dashed arrows represent reflected ones, which can be either blocked (state 0) or allowed to pass (state 1) in each of the stages. Depending on the shutter settings in stages DS1-DS4, bursts of laser pulses with a selected number of femtosecond laser pulses are generated. For example, generation of 16 pulses in the burst corresponds to the shutter settings 1111. Similarly, 8 pulses are generated for 0111, 4 pulses for 0011, 2 pulses for 0001, and a single pulse for 0000. To experimentally confirm the functionality of this pulse-multiplier setup, we investigated the generated pulse bursts by an avalanche photodiode, as depicted in Figs. S1e and S1f.

## B. Switching threshold model and effect of local resistivity change on device resistance

### B1. Switching threshold model

In Fig. S2a, we assume a Gaussian lateral profile for the incident laser pulse, with a half-width  $w \approx 10 \text{ } \mu\text{m}$ . Due to the absorption in CuMnAs epilayer, the pulse intensity decays exponentially with an absorption coefficient of  $\alpha = 3.1 \cdot 10^5 \text{ cm}^{-1}$  [S1]. The resulting energy distribution of the laser light (expressed as energy density per unit volume) within the epilayer is described by

$$U(r, z) = U_0 \cdot e^{-\frac{r^2}{w^2}} \cdot e^{-\alpha z}. \quad (S.B1)$$

Here,  $r$  is the radial distance from the center of the Gaussian profile,  $z$  denotes distance in the epilayer along the laser propagation direction, and  $U_0$  is the amplitude of the energy density.

To evaluate the fluence dependence of the resistive signal (Fig. 3d), we assume that the signal is proportional to the volume of the region in which the energy density in CuMnAs surpasses a threshold value,  $U(r, z) \geq U_{\text{TH}}$ . This volume is given by

$$V_{\text{switched}} = \frac{\pi w^2}{2\alpha} \ln^2(\theta); \quad \theta \geq 1, \quad (S.B2)$$

where  $\theta$ , defined as  $\theta = U_0/U_{\text{TH}}$ , measures the extent to which the threshold energy is exceeded. This quantity can also be represented in terms of the incident laser fluence  $F$  (energy density per unit area) as  $\theta \approx F/F_{\text{TH}}$ , where  $F_{\text{TH}}$  is the threshold fluence. If  $\theta < 1$ , the threshold condition for achieving the switching is not fulfilled, implying  $V_{\text{switched}} = 0$ .

This switched volume can be envisaged as a cap-like shape (see Fig. S2) with a circular base of diameter  $d$ :

$$d = 2w\sqrt{\ln(\theta)}; \quad \theta \geq 1. \quad (S.B3)$$

Fig. S2b demonstrates how the diameter  $d$  expands as the switching threshold is exceeded. Despite the relatively large spot size of the incident laser pulse, a considerably smaller region can be switched.

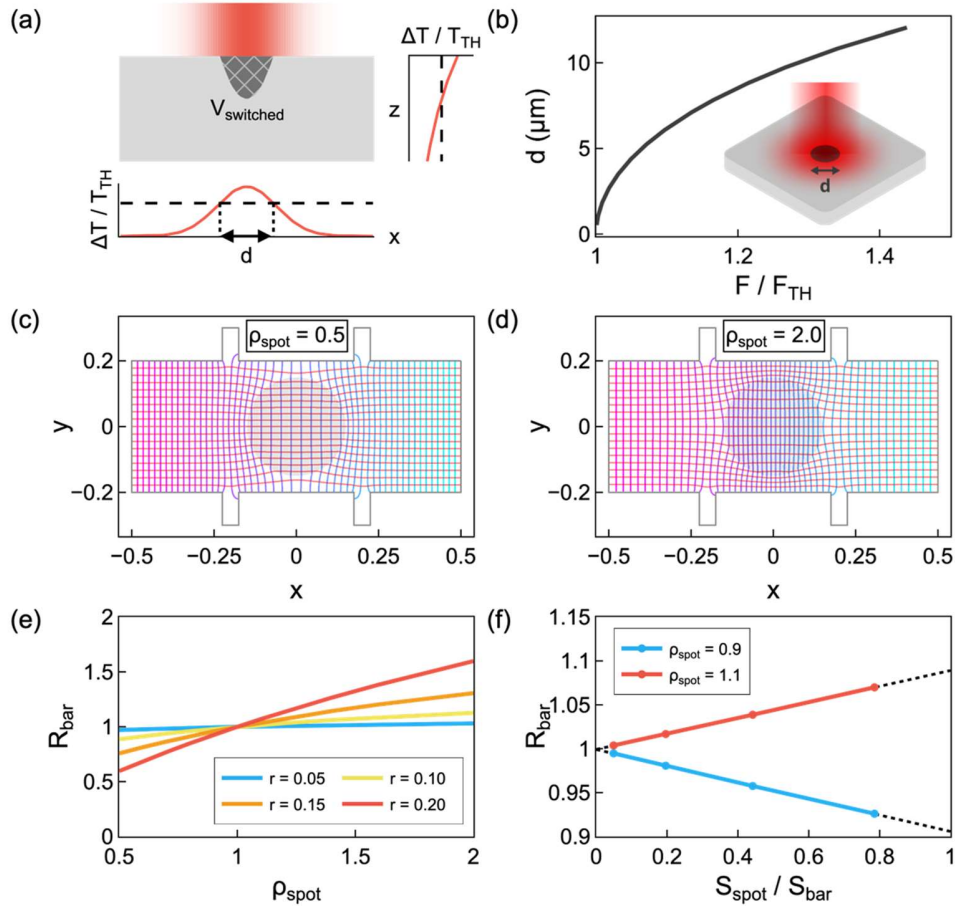


**Fig. S2 | Linear proportionality between the measured resistive signal and the volume of area with changed resistance.** **a**, The incident laser pulse with a Gaussian lateral ( $x$ ) profile is absorbed in the CuMnAs epilayer with an exponentially decaying intensity profile in the  $z$ -direction. The volume  $V_{\text{switched}}$  represents the region where the laser-pulse-induced temperature increase  $\Delta T$  of CuMnAs exceeds the threshold temperature  $T_{\text{TH}}$ . This volume can be visualized as a cap-like structure with a circular base of diameter  $d$ . **b**, The dependence of  $d$  on fluence  $F$ , expressed relative to the value of the threshold fluence  $F_{\text{TH}}$ . Note that despite a relatively large spot size of the incident laser pulse ( $w = 10 \mu\text{m}$ ), a considerably smaller region of CuMnAs can be switched. **c**, Examples of potential distribution and the corresponding current lines in a device structure with a circular spot in the middle (with a radius  $r = 0.15$ ), where the local resistivity  $\rho$  is decreased from  $\rho = 1.0$  to  $\rho = 0.5$  or **d**, increased from  $\rho = 1.0$  to  $\rho = 2.0$ . **e**, For a fixed spot radius  $r$ , the calculated apparent resistance  $R_{\text{bar}}$  of the device scales monotonously with the resistivity inside the spot  $\rho_{\text{spot}}$ . **f**, For a fixed value of  $\rho_{\text{spot}}$ , which deviates weakly from that in the rest of the device, the apparent resistance scales linearly with the spot area  $S_{\text{spot}} = \pi r^2$ .

## B2. Estimation of threshold switching energy

Determining the switching threshold fluence  $F_{\text{TH}}$  enables us to estimate the minimal excitation energy required to induce the switching in CuMnAs. Fluence threshold  $F_{\text{TH}} = 18.5 \text{ mJ/cm}^2$  (evaluated further using method in Part C) corresponds to  $\approx 60 \text{ nJ}$  energy per pulse incident on the surface of the CuMnAs wafer. Taking into account the reflectance of the wafer  $R \approx 40\%$  (see Fig. 6c in Ref. S1), the total energy delivered by the single laser pulse at switching threshold  $\epsilon_{\text{TH}}$  is  $\approx 36 \text{ nJ}$ . Considering the energy distribution of the laser light  $U(r, z)$  within the epilayer described by Eq. (S.B1), the total delivered energy  $\epsilon_{\text{TH}}$  can be expressed as

$$\epsilon_{\text{TH}} = \int_V U(r, z) dV = \frac{\pi w^2}{\alpha} U_{\text{TH}}, \quad (\text{S.B4})$$

where  $U_{\text{TH}}$  is the amplitude of the energy density at switching threshold. Consequently, the threshold energy density can be evaluated as  $U_{\text{TH}} \approx 3.5 \text{ kJ/cm}^3$ .

## B3. Effect of local resistivity change on device resistance

The assumption, mentioned in Part B1, that the resistive signal measured across the device structure is linearly proportional to the volume of the switched area with altered resistance, is not self-evident. To validate this, we conducted simulations modelling a similar situation. Considering the relative thickness of the utilized epilayers ( $\sim \text{nm}$ ) compared to the lateral dimensions of the device ( $\sim \mu\text{m}$ ), simulations were executed in 2D, neglecting the effect of depth. Potential and current distributions were calculated using the finite-element method in a bar-shaped device structure with current contacts at its left and right edges, and with a pair of thin vertical arms to probe the potential drop along the sample, see Figs. S2c and S2d. This potential drop and the calculated total current were utilized to evaluate the four-point (apparent) resistance of the device. The true resistivity of the device material was assumed to be non-uniform: equal to 1.0 everywhere except within a circular spot in the middle of the device, where the resistivity was locally increased (Fig. S2c) or decreased (Fig. S2d). The calculated dependences of the apparent resistance  $R_{\text{bar}}$  on the spot resistivity and spot size are shown in Figs. S2e and S2f, respectively. It indicates that when the change in the spot resistivity  $\rho$  is relatively small (here plus or minus 10% of the value in the unperturbed material), the device resistance scales linearly with the spot area,  $S_{\text{spot}} = \pi r^2$ , and approaches the spot resistivity if the spot covers the whole area between the potential probes  $S_{\text{bar}}$ .

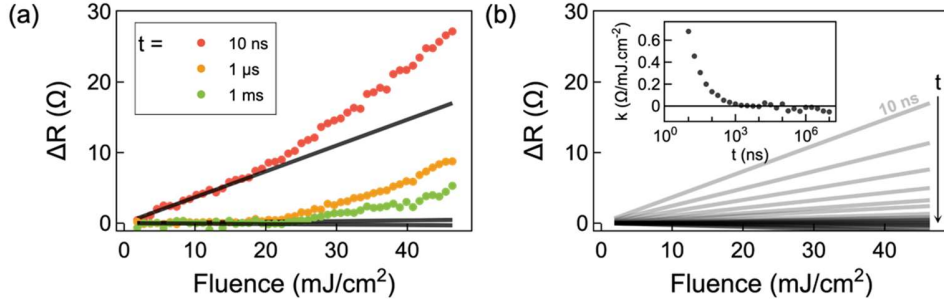
### C. Single-pulse method: Separation of switching and heat contributions from measured resistance change

Fig. 3b presents as-measured oscilloscope data for three selected fluence values of the incident single laser pulse in a device fabricated from a 20-nm-thick CuMnAs epilayer. The major resistive signal following the incidence of the laser pulse can be attributed to the light-induced increase in the sample's temperature. This excess heat dissipates entirely in  $\approx 1 \mu\text{s}$ , as apparent in the data for a fluence of  $20 \text{ mJ/cm}^2$  in Fig. 3b. If a specific laser pulse fluence threshold is exceeded, a new long-lived resistive signal appears, which persists even in the time region where the excess heat is fully dissipated – see data for fluences  $30 \text{ mJ/cm}^2$  and  $40 \text{ mJ/cm}^2$  in Fig. 3b. We ascribe this persistent component to the switching signal. As evident from Fig. 3b, the heat and switching signals are intermixed for times  $< 1 \mu\text{s}$ , and the challenge lies in separating their contributions to the measured resistive signals.

Fig. S3a presents the same data set as in Fig. 3b, but it is plotted as a function of fluence  $F$  for three selected times  $t$  after the incidence of the laser pulse. The data exhibit a characteristic onset with a fluence approximately at  $20 \text{ mJ/cm}^2$ . In addition, there is also a linear background, particularly apparent for short times  $t$  after the incidence of the laser pulse (black lines in Fig. S3a). This background can be attributed to the device resistance change due to temperature increase, which can be approximated by a linear function from  $300 \text{ K}$  to  $\approx 400 \text{ K}$  (see Fig. S4a). The energy delivered to CuMnAs by the laser pulse is characterized by its fluence and, therefore, the heat contribution to the resistance change can be approximated by

$$\Delta R_{(\text{heat})} \sim k * F. \quad (S.C1)$$

Here,  $k$  represents the slope of the linear background. Fig. S3b displays these linear backgrounds for various times  $t$ , fitted for fluences up to  $15 \text{ mJ/cm}^2$ . The inset of Fig. S3b depicts the time evolution of the slope  $k$ , which represents a measure of the excess heat in the studied device. This indicates that the heat is fully dissipated within  $\approx 1 \mu\text{s}$  after the impact of the laser pulse.



**Fig. S3 | Separation of the heat-related resistive signal appearing as a linear background in the as-measured data.** **a**, The as-measured fluence dependence of resistive signal change  $\Delta R$  at three different times  $t$  after the incidence of a single laser pulse (dots) in a device fabricated from a 20-nm-thick CuMnAs epilayer. The linear backgrounds (lines) are attributed to the heat contributions to the resistive signal. These backgrounds were determined by fitting the data up to a fluence of 15 mJ/cm<sup>2</sup> using Eq. (S.C1). **b**, The linear backgrounds at various times  $t$ . Inset: The time evolution of the slope  $k$  of the linear background, representing the measure of excess heat in the investigated device. The heat is fully dissipated within  $\approx 1 \mu\text{s}$  after the impact of the laser pulse.

The switching contribution to the device resistance can be determined by subtracting the linear background from the as-measured data, as shown in Fig. 3d. By re-plotting the data as a function of time  $t$ , this method allows us to deduce the time evolution of heat and switching separately, as depicted in Figs. 3e and 3f. The relaxation of the switching signal can be described by the Kohlrausch stretched exponential [S2]:

$$\Delta R_{\text{(switching)}}(t) \sim A_{S1} e^{-\left(\frac{t}{\tau_{S1}}\right)^{0.6}} + A_{S2} e^{-\left(\frac{t}{\tau_{S2}}\right)^{0.6}} \quad (\text{S.C2})$$

with two dominant components characterized by different relaxation times  $\tau_{S1}$ ,  $\tau_{S2}$  and corresponding weights  $A_{S1}$ ,  $A_{S2}$ . These relaxation times are temperature dependent, with slow and fast room-temperature relaxation times in the approximate ranges of  $\sim 10$  s and  $\sim 10$  ms, respectively (see Fig. 4 in Ref. S2). The relaxation of the switching signal in Fig. 3f is described by the fast component with a relaxation time of  $\approx 4.5$  ms, whereas the slow component is treated as a constant within the measured 10 ms time window.

Although the excess heat in the sample apparently scales with the energy delivered by the light pulse, the linear scaling of the resulting resistive signal according to Eq. (S.C1) is not obvious. Fig. S4a displays the temperature dependence of CuMnAs resistance, measured in a separate electrical experiment during which the sample underwent a gradual heating process. Here, the Néel temperature  $T_N \approx 453$  K was estimated by evaluating the inflection point of this dependence. The

measured resistance change is linear in temperature approximately up to  $\approx 400$  K (as shown by the black line). The inset of Fig. S4a presents the data after subtracting the linear function to emphasize the existence of a non-linear component in the measured dependence. Consequently, the linear scaling of the resistive signal following Eq. (S.C1) applies only if temperature fluctuations within the sample remain relatively low (i.e., when the temperature increase from 300 K remains below  $\approx 400$  K). Fig. S4b presents the fluence dependence of resistive signal at the moment of the laser pulse impact (i.e., at the peak of the resistive signal change observed at  $t = 0$  ns; see also Fig. S5). The depicted value of the fluence threshold  $F_{TH}$  was determined using the switching threshold model (see Fig. 3d and Supplementary Part B). As clearly apparent from this figure, even a laser pulse with a fluence below the switching threshold can significantly elevate the sample's temperature at the moment of incidence, leading to a non-linear temperature dependence of the measured resistance. The non-linear region can be again identified by subtracting a linear function from the measured dependence, which is shown in the inset of Fig. S4b. Overall, the similarities between insets in Fig. S4a and Fig. S4b suggest that there exists a relationship between the fluence threshold  $F_{TH}$  and the Néel temperature  $T_N$ .

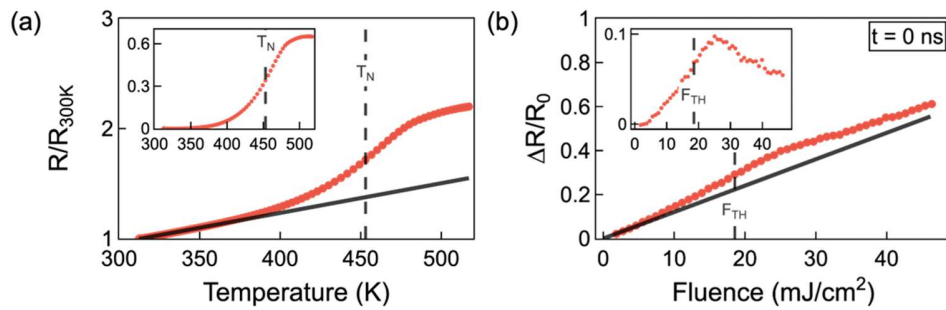


**Fig. S4 | Dependence of the heat-related resistive signal on sample temperature and delivered laser pulse energy.** **a**, The temperature dependence of CuMnAs resistance (dots), normalized to the room-temperature value, as observed in an independent electrical experiment in which the sample was gradually heated. The Néel temperature  $T_N \approx 453$  K was deduced by determining the inflection point in the obtained dependence. The black line represents the linear dependence in the temperature region up to  $\approx 400$  K. Inset: The non-linear component of the relative resistance change obtained by subtracting the linear background from the measured data depicted in the main figure. **b**, The fluence dependence of the resistive signal  $\Delta R$ , normalized to the base resistance  $R_0$ , at the moment of the laser pulse impact ( $t = 0$  ns). The fluence threshold  $F_{TH}$  is evaluated using the switching threshold model (see Supplementary Part B). Inset: The non-linear component of the signal is obtained by subtracting the linear background (line), fitted for fluences up to  $5 \text{ mJ/cm}^2$ , from the data.

Finally, we would like to comment on the overall time resolution of this procedure, which enables the separation of switching and heat contributions from the as-measured resistances. To be applicable, the linear relationship between the laser-pulse-induced sample heating and the resulting resistance change, as described by Eq. (S.C1), has to be fulfilled. In a 20-nm-thick CuMnAs epilayer, this is the case for times  $t \geq 10$  ns, when the vast majority of heat deposited to the sample is already dissipated (see Fig. 3e) and, presumably, the temperature of the excited spot is reduced below  $\approx 400$  K (see Fig. S4a). Technically, this technique can be applied also for shorter times but the reliability of the obtained outputs is questionable. Therefore, we depicted this unreliable time range by a grey color in Fig. 3e and 3f.

#### **D. Double-pulse method: Heat accumulation and separation of resistive signals for two mutually-time-delayed laser pulses**

The CuMnAs device structure can serve as a memory element, capable of encoding analog information using a pair of femtosecond laser pulses mutually-time-delayed on ultrafast timescales (see Fig. 4). The writing process in these devices is governed by the ultrafast heat dynamics in CuMnAs, as schematically illustrated in Fig. 4b. Depending on the pulse-pair mutual time-delay, the accumulated heat in CuMnAs can lead to a temperature increase above a certain threshold temperature  $T_{\text{TH}}$  and, consequently, to the switching. In this Chapter we explore this effect experimentally. Moreover, we illustrate how this two-pulse experiment can be utilized to deduce switching related resistivity dynamics, which is in a very good agreement with the results of a single-pulse method depicted in Fig. 3 and analyzed in Supplementary Part C.

As extensively discussed in Supplementary Part C, the absorption of a femtosecond laser pulse leads to a transient temperature increase in the CuMnAs epilayer. This temperature alternation consequently results in a time-dependent resistivity change (cf. Fig. S4) detected in our experiment (see Fig. S5). Due to the limited bandwidth of the electrical setup, the ultrafast (picosecond) local heating of the material (see Figs. 4e and 4f) after laser pulse impact is apparent in the measured resistivity waveforms as a peak with a  $\approx 2$  ns-long rising edge, representing the time resolution of our electrical experiment depicted as a gray area in Fig. S5a. (The sub-nanosecond heat dynamics is discussed in detail in Supplementary Part E.) Up to  $\approx 10$  ns, the laser pulse-induced resistivity change is dominated by the heat contribution (cf. Figs. 3e and 3f)



originating in sample's increased temperature. As the resistivity is a monotonous function of the sample temperature (see Fig. S4a), the early stages of the as-measured resistivity dynamics depicted in Figs. S5a and S5b can be regarded, to some extent, as a visualization of the temperature dynamics in the sample. In particular, the "summation" of heats delivered by a pair of laser pulses, mutually delayed by a time  $\Delta t$ , can be studied experimentally directly in a time domain. Here, we use a notation where laboratory time  $t = 0$  is defined by the position of the resistivity peak induced by the impact of the second laser pulse, which is denoted as  $B$  in Fig. S5. If the first laser pulse, denoted as  $A$ , is incident on the sample before pulse  $B$ , we consider their mutual time delay  $\Delta t > 0$ . In this manner we can deduce the evolution of their *combined* effect in a laboratory time  $t$ , as depicted in Figs. S5 and S6, and discussed in detail below.

Experimentally, the resistivity changes induced by two identical  $\Delta t$ -time-delayed laser pulses can be recorded either for the separate impact of each pulse (waveforms  $A$  and  $B$  in Figs. S5a and S5b) or when both pulses are present (waveform  $AB$ ). Waveform  $A+B$  represents the arithmetic sum of waveforms  $A$  and  $B$ . Fig. S5a demonstrates the heat accumulation following the incidence of two laser pulses with a large time-delay  $\Delta t = 4$  ns. In this case, the majority of the heat delivered by pulse  $A$  dissipates before the incidence of pulse  $B$ . As a result, the cumulative heat does not surpass the threshold level (schematically depicted as a dashed horizontal line) necessary to switch the sample. Consequently, the arithmetic sum of individual heat contributions from pulses  $A$  and  $B$  closely matches the measured waveform  $AB$ . In contrast, for a small time-delay between pulses ( $\Delta t = 10$  ps in Fig. S5b), the cumulative heat exceeds the threshold, and the arithmetic sum of the waveforms  $A$  and  $B$  deviates considerably from the waveform  $AB$  measured when both pulses are present. Despite the fact that neither pulse  $A$  nor pulse  $B$  can trigger switching individually, the combined effect of this pulse-pair can. Hence, the difference between waveforms  $AB$  and  $A+B$  corresponds to the switching component in the resistive signal

$$\Delta R_S(t) \sim \Delta R_{AB}(t) - [\Delta R_A(t) + \Delta R_B(t)]. \quad (S.D1)$$

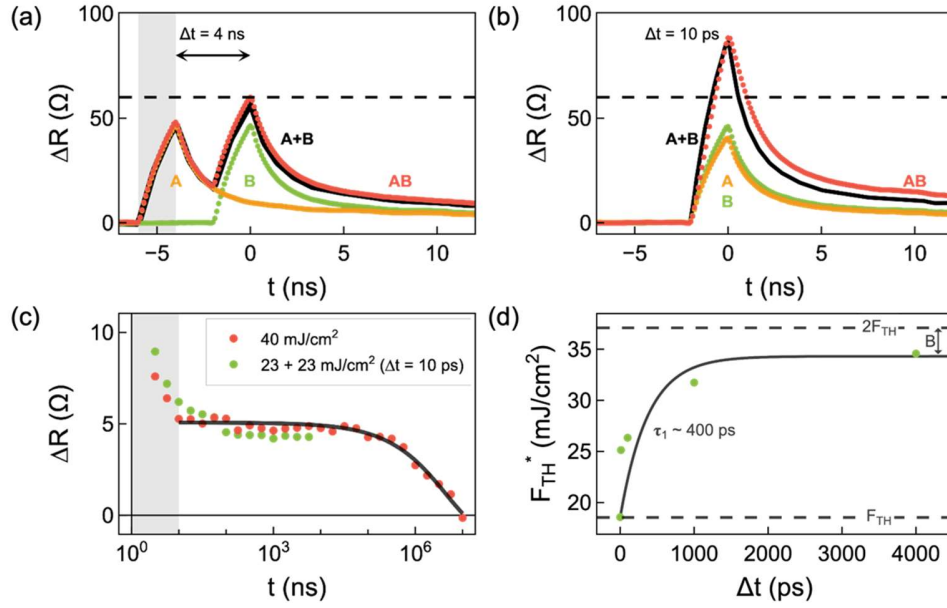


**Fig. S5 | Accumulation of heat from two identical, mutually-time-delayed laser pulses in a device prepared from a 20-nm-thick CuMnAs epilayer.** **a**, Time-resolved resistive signals measured for two identical laser pulses with fluence 20 mJ/cm<sup>2</sup> and a mutual time-delay  $\Delta t = 4$  ns. The waveforms  $A$  and  $B$  depict the effect of each pulse's incidence individually, while the waveform  $AB$  represents the resistivity change when both pulses are present. The waveform  $A+B$  represents the arithmetic sum of waveforms  $A$  and  $B$ . The dashed horizontal line illustrates the resistive threshold level which needs to be surpassed to trigger the measurable switching in the sample. The electrical measurements' time resolution of  $\approx 2$  ns is depicted as a grey area (see text). **b**, Same as **a**, but for  $\Delta t = 10$  ps. Again, the laser pulses are unable to trigger the detectable switching individually. However, their combined effect exceeds the threshold  $\Delta R_{TH}$  (waveform  $AB$ ). The difference between waveforms  $AB$  and  $A+B$  is due to the resistivity change induced by the switching, which is depicted in **c** as green points. Red points in **c** represent resistivity dynamics deduced from the single-pulse method described in Supplementary Part C. The gray area denotes the time window where the applicability of the used methods is questionable (see Supplementary Part C). The black line describes the relaxation of the switching signal using the Kohlrausch stretched-exponential model (see Supplementary Part C). **d**, The total delivered fluence threshold  $F_{TH}^*$  for a pair of laser pulses shown as a function of their mutual time delay (points); see Fig. S6 for the measured data from which the values of  $F_{TH}^*$  were deduced. The threshold ranges from the single-pulse threshold value  $F_{TH}$ , for time-overlapping pulses, to  $2F_{TH}$  for very distant pulses. The line represents the theoretical model of Eq. (S.D3) with a thermal relaxation time constant  $\tau_1 \sim 400$  ps, see text.

The applicability of this approach, which is based on the assumption that the resistivity is approximately linearly dependent on the delivered heat (i.e., on the increase in sample temperature), is illustrated in Fig. S5c. Here we compare results from this double-pulse method with those of the single-pulse method described in Supplementary Part C. Clearly, the dynamics

of the switching signals derived from both methods show a very good agreement. Note that in the case of the double-pulse method, the total double-pulse fluence  $F^*$  (defined as a sum of the fluences of both pulses) exceeds the single-pulse fluence  $F$  necessary to achieve comparable resistive signals (e.g., 46 vs. 40 mJ/cm<sup>2</sup> for  $\Delta t = 10$  ps in Fig. S5c). This difference in total delivered energy originates from the partial dissipation of heat from the first pulse before the incidence of the second.

The deduced dynamics of switching signals for three values of  $\Delta t$  are displayed in Figs. S6a, 6c and 6e. The corresponding fluence dependencies, depicted in Figs. S6b, 6d, and 6f, reveal the aforementioned inter-pulse partial heat dissipation effect, which is apparent as an increase of the total delivered fluence threshold  $F_{\text{TH}}^*$  with  $\Delta t$ . This dependence is summarized in Fig. S5d as points. Intuitively, the plausible extreme values of  $F_{\text{TH}}^*$  (represented as dashed horizontal lines in Fig. S5d) can be understood as follows. If  $\Delta t$  approaches 0 ps, the situation evolves towards a single laser pulse scenario, where  $F_{\text{TH}}$  is sufficient to switch the sample, consequently leading  $F_{\text{TH}}^*$  to converge to  $F_{\text{TH}}$ . Conversely, for  $\Delta t$  considerably exceeding the heat dissipation times, the effect induced by both pulses become entirely independent. Now, to achieve a switching, each pulse has to exceed the threshold  $F_{\text{TH}}$  independently, thereby causing  $F_{\text{TH}}^*$  to converge towards  $2F_{\text{TH}}$ . To derive the expected dependence between these two extreme values, we need to estimate the energy, delivered by the first pulse, that partially dissipates before the impact of the second pulse at time delay  $\Delta t$ . This can be expressed as

$$\Delta E(\Delta t) = A - \left( (A - B)e^{-\frac{\Delta t}{\tau_1}} + B \right) \quad (S.D2)$$

Here,  $A$  is the amplitude of the heat energy delivered by the pulse, and  $B$  is the residual heat background (see Fig. S9a and Supplementary Part E for a detailed description). If the first pulse is delivering the threshold fluence  $F_{\text{TH}}$ , the energy dissipated after  $\Delta t$ , which the second pulse must compensate for, can be expressed as  $\Delta E_{\text{TH}}(\Delta t) = \Delta E(\Delta t \mid A=F_{\text{TH}}, B=B_{\text{TH}})$ . The total fluence threshold is then:

$$F_{\text{TH}}^*(\Delta t) = F_{\text{TH}} + \Delta E_{\text{TH}}(\Delta t) = F_{\text{TH}} + (F_{\text{TH}} - B_{\text{TH}}) * \left( 1 - e^{-\frac{\Delta t}{\tau_1}} \right) \quad (S.D3)$$

The model described by Eq. (S.D3) was utilized to generate the solid line in Fig. S5d using values  $F_{TH} = 18.5 \text{ mJ/cm}^2$  (obtained from the switching threshold model described in Supplementary Part B),  $\tau_1 = 375 \text{ ps}$  (inferred from the heat dissipation model in Supplementary Part E), and a fitted value of  $B_{TH} = 2.8 \text{ mJ/cm}^2$ .

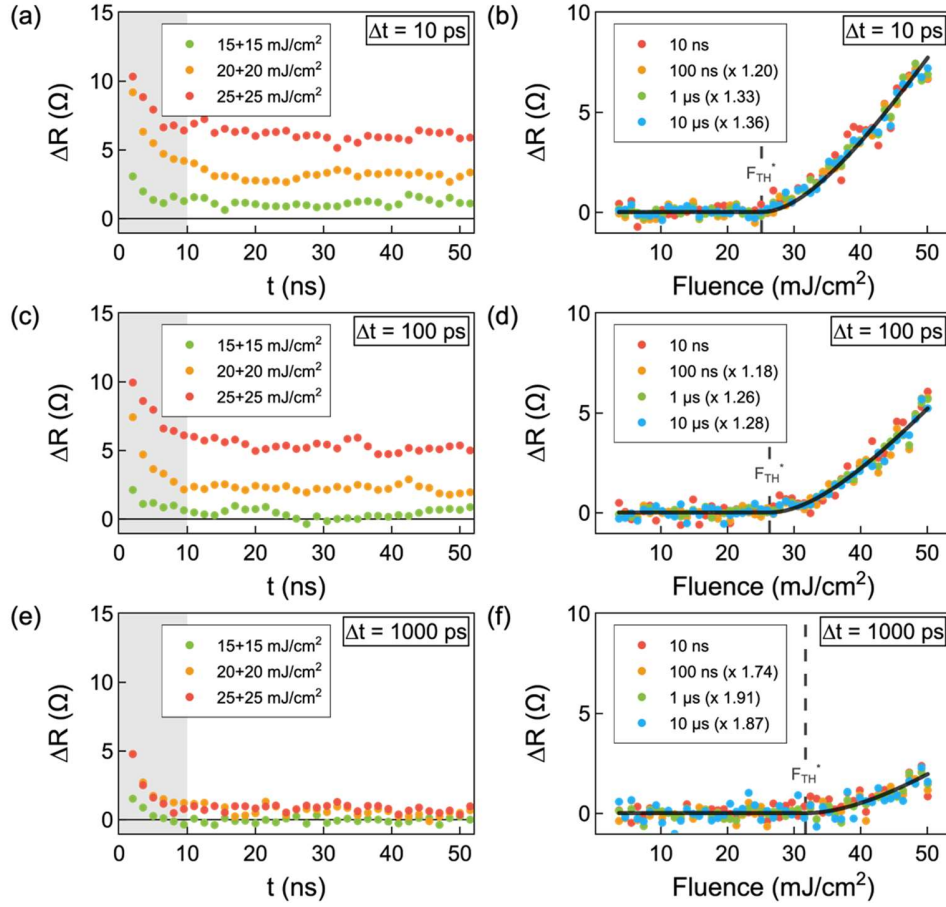


**Fig. S6 | Switching signals in a device prepared from a 20-nm-thick CuMnAs epilayer sample measured by the double-pulse method.** **a**, Dynamics of switching signals obtained for a time delay between pulses  $\Delta t = 10 \text{ ps}$  and depicted fluences. **b**, Switching contributions of resistive signals, corresponding to the same  $\Delta t$  as in **a**, shown as a function of the total fluence from both pulses for depicted times  $t$  after the impact of the second pulse. The data are multiplied by the indicated factors to show their common fluence dependence. The line represents a fit using a theoretical threshold model (see Supplementary Part B), defining the value of the total fluence threshold  $F_{TH}^*$ . **c**, **d**, and **e**, **f**, are analogous to **a** and **b** with  $\Delta t = 100 \text{ ps}$  and  $1000 \text{ ps}$ , respectively.

In conclusion, this Chapter aimed to illustrate that a rather complex experimental data measured using a pair of mutually-time-delayed laser pulses (Figs. S5 and S6) can be modeled well by a simple phenomenological model describing the heat dissipation dynamics in CuMnAs. The consequences of this are discussed in detail in Supplementary Part E.

## E. Heat dissipation dynamics

Optical writing experiments employing a pair of laser pulses, as depicted in Fig. 4, reveal that the switching in CuMnAs epilayers is governed by ultrafast heat dynamics: incident optical pulses always heat the sample, but they trigger the writing only when a specific excitation threshold is surpassed (cf. Fig. 4b). However, deducing the heat dynamics directly from these measurements is not straightforward. The complexity arises because  $\Delta R$  signal is influenced by the nonlinear onset response (see Fig. 3d), making it highly sensitive to exceeding the threshold. A clear manifestation of this enhanced sensitivity can be observed, for example, in a device prepared from a 20-nm-thick CuMnAs epilayer, where the half-width at full maximum of the  $\Delta R$  dependence on  $\Delta t$  is approximately 90 ps (see Fig. 4c), in contrast to the thermal dissipation time  $\tau_1 \approx 400$  ps, measured in an independent experiment depicted in Fig. 4f.

### E1. Effective switching fluence in the double pulse experiment

To address this, we introduce the concept of the effective switching fluence  $F_{\text{eff}}(\Delta t)$ . This quantity represents the fluence of a single laser pulse that would generate the same  $\Delta R$  signal as a laser pulse-pair with a given mutual-time-delay  $\Delta t$ .

Converting the resistive signal measured after the incidence of a laser pulse-pair  $\Delta R_{2p}(\Delta t)$  (double-pulse signal in the following) to  $F_{\text{eff}}(\Delta t)$  requires determining an analytical formula  $F(\Delta R_{1p})$ , which is relating the fluence  $F$  and the resistive signal measured after the incidence of a single laser pulse  $\Delta R_{1p}(F)$  (single-pulse signal in the following). Although the threshold model describing  $\Delta R_{1p}(F)$  (see Supplementary part B) can, in principle, be utilized for this purpose, it does not guarantee the needed one-to-one invertible relationship between  $F$  and  $\Delta R_{1p}$ . To do so, we employed a sigmoidal function:

$$\Delta R_{1p}(F) \sim \frac{A_S}{1 + e^{-w_S(F-F_C)}} \quad (S.E1)$$

with a sigmoid amplitude  $A_S$ , width  $w_S$  and center  $F_C$ . Even though we do not ascribe any specific physical meaning to this model, it offers a good fit to the data. To determine the parameters of the sigmoidal model, we fitted  $\Delta R_{1p}(F)$  at multiple time points  $t$  (see Fig. 3d) after the incidence of a single laser pulse, as illustrated in Figs. S7a, 7b, and 7c for a device prepared from a 20-nm-thick CuMnAs epilayer. Considering that apart from a scaling factor, the fluence dependencies at various times  $t$  maintain the same shape (see Fig. 3d), we defined the sigmoid width  $w_S$  and the center  $F_C$  as global ( $t$ -independent) parameters, and the scaling factor  $A_S(t)$  as a  $t$ -dependent parameter. Finally, we converted the double-pulse signal  $\Delta R_{2p}(\Delta t)$  to the effective switching fluence  $F_{\text{eff}}(\Delta t) = F(\Delta R_{2p}(\Delta t))$  using the  $F(\Delta R_{1p})$  relation obtained by inverting the formula (S.E1), as shown in Fig. S7d. Note that this approach is applicable only in a region of non-zero  $\Delta R_{2p}$  values and, hence the  $x$ -scale in Fig. S7d is considerably shorter than that in Fig. 4c. Fig. S8 illustrates the same process for a device prepared from a 50-nm-thick CuMnAs epilayer.

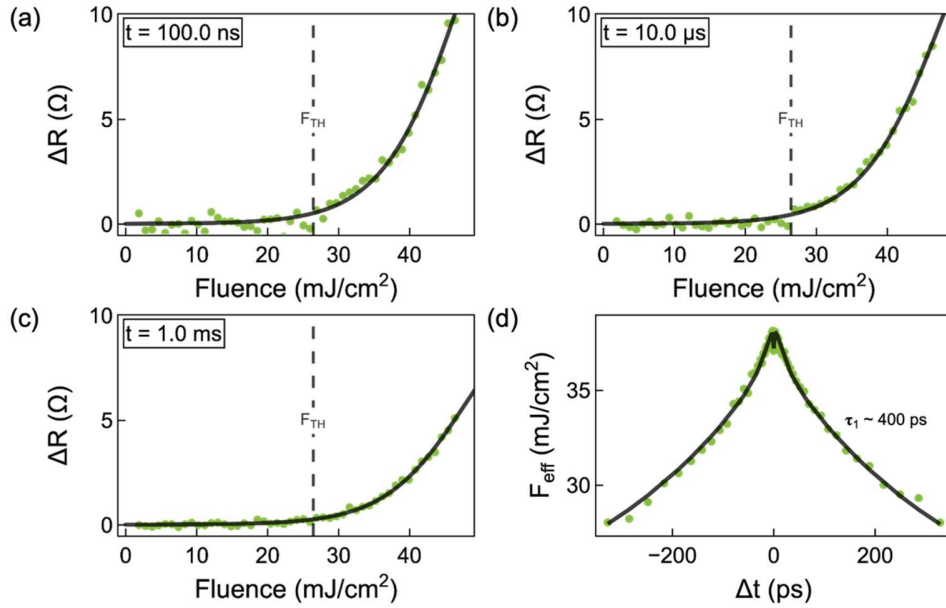


**Fig. S7 | Conversion of the measured double-pulse resistive signal to the Effective Switching Fluence  $F_{\text{eff}}$  in a device prepared from a 20-nm-thick CuMnAs epilayer.** **a - c**, Fluence dependence of  $\Delta R$  at three times  $t$  after the impact of a single laser pulse (dots). Data are fitted by Eq. (S.E1) to establish an analytical relationship between the fluence and  $\Delta R$  (line), which is used to convert the double-pulse data into  $F_{\text{eff}}$ . The vertical line depicts the position of the fluence threshold  $F_{\text{TH}}$ . **d**, Obtained  $F_{\text{eff}}$  as a function of a mutual-time-delay  $\Delta t$  between the pair of laser pulses (dots). The line is a fit by Eq. (S.E4), yielding the depicted value of the heat dissipation time constant  $\tau_1$ .

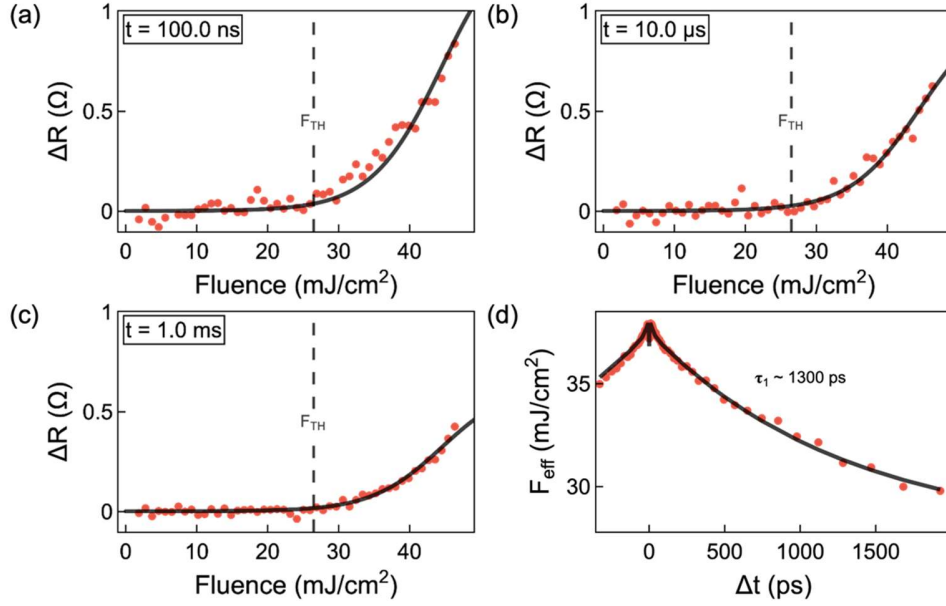


**Fig. S8 | Conversion of the measured double-pulse resistive signal to the Effective Switching Fluence  $F_{\text{eff}}$  in a device prepared from a 50-nm-thick CuMnAs epilayer. a - d, Same as in Fig. S7 but for a 50-nm-thick CuMnAs epilayer.**

## E2. Heat dynamics model

The effective switching fluence  $F_{\text{eff}}$  in the double-pulse experiment estimates the effective energy delivered by the pulse-pair to the CuMnAs epilayer at the time of the arrival of the second pulse. Prior to the incidence of the second pulse, the heat originating from the first pulse partially dissipates. Assuming a monoexponential dissipation of the delivered heat from the epilayer to the substrate, characterized by a thermal relaxation time  $\tau_1$ , the relationship between  $F_{\text{eff}}$  and the pulse-pair delay  $\Delta t$  can be conceptually represented as:

$$F_{\text{eff}}(\Delta t) = F_1 e^{-\frac{\Delta t}{\tau_1}} + F_2, \quad (S.E1)$$

where  $F_1$  and  $F_2$  correspond to the incident fluences from the first and second laser pulses, respectively.

For our specific experimental conditions, we employed the phenomenological model depicted in Fig. S9a. We utilized identical laser pulses with fluences  $F_1 = F_2 = A$ , which are insufficient to trigger switching individually. However, when combined in a time overlap ( $\Delta t = 0$ ), they result in an effective fluence of  $2A$ , well above the switching threshold. Apart from the heat dissipation from the epilayer to the substrate, characterized by  $\tau_1$  on  $\sim$  ns timescales (cf. Fig. 4f),

we are also considering the heat dissipation from the substrate to the environment (e.g., to a sample holder and air), which occurs over longer timescales (see Fig. 3e). Therefore, on the ns timescales relevant for the double-pulse experiments, this residual heat background  $B$  can be considered as a constant. Consequently, before the incidence of the second laser pulse, the heat originating from the first pulse dissipates as  $\sim (A-B)\exp(-t/\tau_1)+B$  (see Fig. S9a), and the effective switching fluence  $F_{\text{eff}}(\Delta t)$  can be represented by the following phenomenological model:

$$F_{\text{eff}}(\Delta t) \sim \left( (A - B)e^{-\frac{\Delta t}{\tau_1}} + B \right) + A. \quad (\text{S.E2})$$

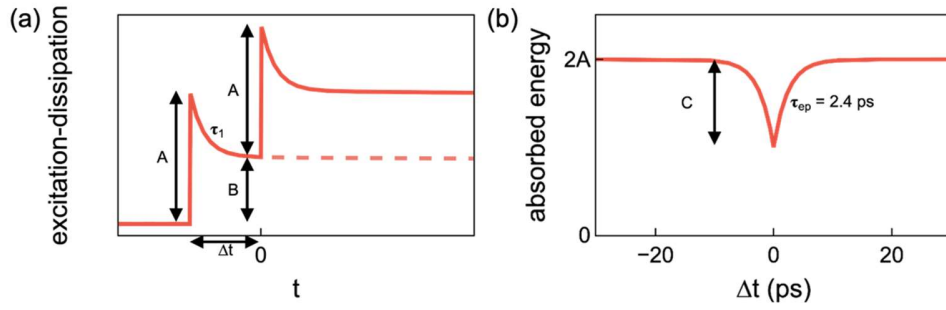


**Fig. S9 | Illustration of Heat Dynamics in a CuMnAs Epilayer.** **a**, The schematic illustration of the heat dynamics within a CuMnAs epilayer following the incidence of a pair of laser pulses separated by a mutual-time-delay  $\Delta t$ . Each individual laser pulse delivers heat energy of amplitude  $A$ , which is subsequently dissipated to the substrate with a thermal relaxation time  $\tau_1$ . Considering that the dissipation of heat from the substrate to the environment occurs over significantly longer timescales, the residual heat background  $B$  can be treated as a constant on ps to ns timescales. **b**, Energy delivered to the epilayer by a pair of laser pulses at 1030 nm. The first pulse transiently increases the CuMnAs reflectivity, which is sensed by the second pulse, that results in a transient reduction of the total absorbed energy.

The heat dissipation model given by Eq. (S.E2) allows us to obtain the thermal relaxation times  $\tau_1$  from  $F_{\text{eff}}(\Delta t)$  data in Fig. S7d and Fig. S8d for 20-nm-thick and 50-nm-thick CuMnAs epilayers, respectively. However, this model fails in describing the data near the zero-time overlap of the pulse pair (see Insets in Fig. 4c and 4d), necessitating an extension of the model in this ultrafast delay time range, which is based on independent pump-probe measurements of transient reflectivity shown in Fig. 4e. As depicted in the inset of Fig. 4e, at 1030 nm, which is the wavelength of laser pulses used for the single-pulse and double-pulse experiments, absorption of a first (pump) laser pulse transiently increases the CuMnAs reflectivity experienced by the second



(probe) pulse, which decays on a  $\sim$  ps timescale. The mechanism responsible for this transient ultrafast reflectivity increase can be identified by a non-degenerate pump-probe experiment [S1] depicted in Figs. 4e and 4f (see the Methods section for experimental details). The photoexcitation of a metal by an intense femtosecond laser pulse excites the electron distribution out of equilibrium on a time scale much shorter than the electron–phonon interaction time. The resulting non-thermal population of electrons thermalizes rapidly by electron–electron scattering processes. Consequently, a thermalized electron system, which can be described by a Fermi distribution with an elevated electron temperature, is formed within  $\approx 100$  fs after the impact of the pump pulse. On a picosecond time scale, the excess energy is dissipated from the electron system to the lattice by electron–phonon scattering processes, which leads to an increase in the lattice temperature. Finally, on a longer time scale, heat diffusion dissipates the excess energy and the metal returns to the equilibrium state. Importantly, all the above effects lead to a change in optical properties and, therefore, the corresponding characteristic time constants can be evaluated from the measured optical transient signals [S1]. Experimentally, these time constants can be straightforwardly identified in a non-degenerate pump-probe experiment where a time evolution of differential reflectivity  $dR/R$  and differential transmission  $dT/T$  are measured using probe pulses of various wavelengths ( $\lambda$ ) [S1]. The measured reflectivity dynamics can be reproduced by a phenomenological equation [S1]

$$\Delta R/R(\delta t, \lambda) = [\alpha(\lambda)(1 - e^{-\delta t/\tau_{ee}})e^{-\delta t/\tau_{ep}} + \beta(\lambda)(1 - e^{-\delta t/\tau_{ep}})]e^{-\delta t/\tau_l}. \quad (S.E3)$$

The first term, with a spectral weight  $\alpha$ , represents the electronic response with a rise time described by the electron-electron thermalization time  $\tau_{ee}$  and decaying by an energy transfer to the lattice with the characteristic electron-phonon relaxation time  $\tau_{ep}$ . The second term, with a spectral weight  $\beta$ , describes the lattice heating, with the same time constant time  $\tau_{ep}$ , and the thermal relaxation time  $\tau_l$  represents the heat diffusion from the excited area. From the data depicted in Figs. 4e and 4f we deduced the values of the electron-phonon relaxation time in CuMnAs  $\tau_{ep} \approx 2.4$  ps and the heat diffusion time constants  $\tau_l$  for various film thicknesses (see Inset in Fig. 4f), which are fully consistent with the values deduced from the double-pulse experiments.

To be applicable also on ultrafast (ps) times scales, the heat dissipation model given by Eq. (S.E2) has to be modified to include also this transient increase of the sample's reflectivity, which

is reducing the energy absorbed in CuMnAs (with an amplitude  $C$  and time constant  $\tau_{ep}$ ) if the delay time between the laser pulse pair is in a  $\sim$  ps timescale (see Fig. S9b). Moreover, in the measured double-pulse data (Figs. 4c and 4d) we also identified a presence of an additional component with an amplitude  $D$  and time constant  $\tau_x$ . Overall, the revised heat dynamics model is expressed as:

$$F_{\text{eff}}(\Delta t) \sim \left( (A - B)e^{-\frac{\Delta t}{\tau_1}} + B \right) + \left( A - Ce^{-\frac{\Delta t}{\tau_{ep}}} \right) + \left( De^{-\frac{\Delta t}{\tau_x}} \right) \quad (S.E4)$$

The fits by this model to the  $F_{\text{eff}}(\Delta t)$  data for the 20- and 50-nm-thick CuMnAs epilayers are depicted in Figs. S7d and S8d, respectively. The obtained parameters are summarized in Table S1. At present, we do not have any clear physical interpretation of the origin of the heat dissipation component with the amplitude  $D$ , which is observed experimentally in the electrical double-pulse experiments on prepared devices but not in the optical pump-probe experiments on the bare epilayers. Further studies are needed to address this.

**Table S1 | Parameters of the heat dissipation model for 20- and 50-nm-thick CuMnAs epilayers.**

Component	20 nm		50 nm	
	Amplitude (mJ/cm <sup>2</sup> )	Time constant	Amplitude (mJ/cm <sup>2</sup> )	Time constant
A	18.4	$\tau_1 = 375$ ps	18.8	$\tau_1 = 1250$ ps
B	3.2	-	9.0	-
C	1.7	$\tau_{ep} = 2.4$ ps	1.4	$\tau_{ep} = 2.4$ ps
D	2.0	$\tau_x = 20$ ps	0.7	$\tau_x = 20$ ps

## F. Speed limit estimation for STM to LTM information transfer

As described in detail in Part E, we can quantitatively infer time constant  $\tau_l$  from the double-pulse experiments shown in Figs. 4c and 4d, which is in accord with the value deduced independently from pump-probe experiments depicted in Figs. 4e and 4f. From an expression,  $F \exp(-t_{\text{above}}/\tau_l) = F_{\text{TH}}$ , and from the experimental values of  $\tau_l$  and of the switching-threshold fluence  $F_{\text{TH}}$  (see Fig. 3d), we can estimate the time  $t_{\text{above}}$  the antiferromagnet remains excited above the switching threshold after the pulse of fluence  $F$  at a position corresponding to the center of the Gaussian laser beam. As shown in Fig. S10b, we can experimentally resolve switching signals for which  $t_{\text{above}}$  approaches the  $\sim 10$  ps time scale. Therefore, this time can be regarded as an upper estimate of time needed to achieve the information transfer from STM to LTM.

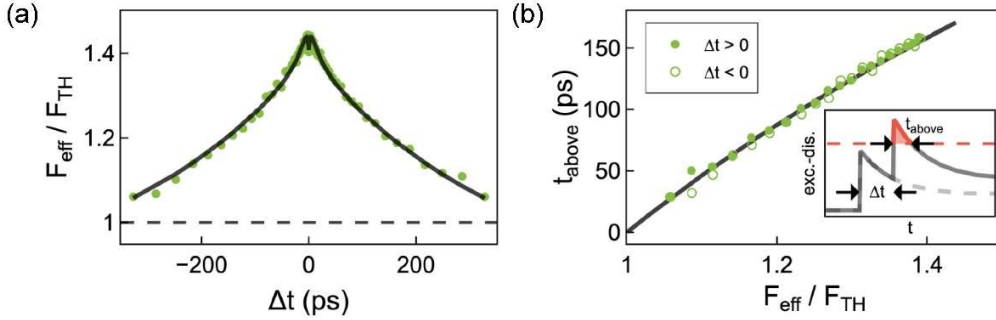


**Fig. S10: Estimation of time needed to achieve the information transfer from STM to LTM from double-pulse experiment.** **a**, Delay-time dependence of  $\Delta R$  measured 0.1 ms after the incidence of the pair of laser pulses in a device made from a 20-nm-thick CuMnAs epilayer (depicted in Fig. 4c) expressed as an effective switching fluence, which represents the fluence required for a single pulse to induce the same  $\Delta R$  as the pair of pulses (see part E for details); the obtained fluences are normalized by the switching-threshold fluence  $F_{\text{TH}}$ . **b**, Time  $t_{\text{above}} = \tau_{\text{th}} \ln(F/F_{\text{TH}})$  the antiferromagnet remains excited above the switching threshold after the pulse as a function of the pulse fluence inferred from data shown in part **a**. Inset: illustration of  $t_{\text{above}}$  in the excitation-dissipation cartoon with the threshold depicted by the red dashed line.

## References

- [S1] Surýnek, M. *et al.* Investigation of magnetic anisotropy and heat dissipation in thin films of compensated antiferromagnet CuMnAs by pump-probe experiment. *Journal of Applied Physics* **127**, 233904 (2020).
- [S2] Kašpar, Z. *et al.* Quenching of an antiferromagnet into high resistivity states using electrical or ultrashort optical pulses. *Nature Electronics* **4**, 30–37 (2021).

[S3] Wadley, P. *et. al.* Antiferromagnetic structure in tetragonal CuMnAs thin films. *Scientific Reports* **5**, 17079 (2015).